RICE UNIVERSITY

Photonic Metamaterials for Color Devices and Deep UV Second Harmonic Generation
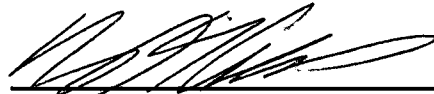
by

Michael Semmlinger

A THESIS SUBMITTED
IN PARTIAL FULFILLMENT OF THE
REQUIREMENTS FOR THE DEGREE

Master of Science

APPROVED, THESIS COMMITTEE

Dr. Naomi J. Halas, Chair
Stanley C Moore Professor of Electrical
and Computer Engineering, Professor of
Biomedical Engineering, Chemistry, and
Physics & Astronomy

Dr. Peter J. Nordlander
Wiess Chair and Professor of Physics &
Astronomy, Professor of Electrical and
Computer Engineering, Materials Science
and Nanomaterials Engineering

Dr. Stephan Link
Professor of Chemistry, Professor of
Electrical & Computer Engineering

HOUSTON, TEXAS
March 2018

ABSTRACT

Photonic Metamaterials for Color Devices and Deep UV Second Harmonic Generation

by

Michael Semmlinger

Photonic Metamaterials are novel materials that consist of subwavelength optical resonators called meta-atoms. They have attracted much attention, due to their ability to control and confine light. In particular, they have promising applications in color generation and nonlinear optics. Here, I give one example for each of these two applications. Chapter one presents an actively tunable full-spectrum device. An array of plasmonic aluminum particles is integrated into a stretchable polymer substrate. Stretching the substrate in either of its two dimensions causes a change in the array period, and therefore changes the associated scattering color. Using a two-dimensional stretching approach, I demonstrate full-spectrum tuning, as well as image switching. In chapter two I present an all-dielectric metamaterial consisting of an array of zinc oxide (ZnO) nanodisks. The material shows a magnetic dipole resonance at around 400nm. When pumped at resonance, the associated field enhancement can be used to generate the second harmonic frequency. This serves as a first demonstration for a simple device for deep UV harmonic generation.

Acknowledgments

Contents

List of Figures

Chapter 1

Actively Tunable Full Spectrum Device

1.1. Introduction

This chapter is based on work that was published in Nano Letters in 2017, with me as one of the first authors [1]. It came out of a collaboration between Dr. Ming-Lun Tseng, Jian Yang, and myself. Dr. Ming-Lun Tseng and I were working under the supervisor of Dr. Naomi Halas. Jian Yang was working under the supervision of Dr. Peter Nordlander. All simulations were performed by Jian Yang using Lumerical FDTD. Dr. Ming-Lun Tseng and I worked on the experimental side together. However, due to considerations of highest efficiency, Dr. Ming-Lun Tseng performed the e-beam lithography by himself, while I focused on the spectral measurements and data analysis.

Generating colors and images with subwavelength optical resonators is a promising and active area of research [2–12]. This is because pixels composed of such

nanostructures open doors to new display technologies with improved spatial resolution[11] and color vibrancy[6,13] compared to traditional approaches. Due to their collective oscillation of conduction band electrons, metallic nanostructures are an excellent way to produce strong, vivid colors[14]. Furthermore, plasmonic resonances in metal nanostructures as well as photonic resonances in dielectric structures can be manipulated in many different ways[15–23]. For example, manipulating the geometry or the inter-particle spacing, allows for control over the resonance position of nanostructures or metamaterials composed of arrays of such structures[6,13,24–26]. They can also be incorporated into microelectromechanical (MEMS) systems[27] or liquid crystal devices(LCD)[3,12,15,28,29]. Even molecular plasmonic devices have been used for color generating devices[30,31].

One promising approach uses flexible polymers, such as polydimethylsiloxane (PDMS) as a substrate to manipulate the inter particle distances. In the following, I will present an aluminum pixel device that can produce colors across the whole visible spectrum, by mechanical deformation of a PDMS substrate. However, first I would like to review in more detail the two most relevant areas of research: aluminum plasmonic pixels, and stretchable plasmonics.

1.1.1. Aluminum Plasmonic Pixels

Aluminum is an ideal metal for a plasmonic pixel device because its high bulk plasma frequency makes its plasmonic resonance tunable from the ultra-violet to the infrared[32,33]. More traditional plasmonic materials like gold or silver have distinct disadvantages. Gold nanostructures can only show quenched colors below

about 520nm because of the onset of interband transitions[13,32]. Silver structures can in principle be used across the entire visible spectrum, but suffer from oxidation problems[13,32]. Aluminum on the other hand forms a self-passivating oxide layer that prevents further oxidation[13]. In addition, it is an inexpensive, earth-abundant, and CMOS compatible material[13,32]. Figure 1.1 shows an example of an aluminum plasmonic pixel device that was reported by Olson et al.[3]. The building blocks for the pixels are aluminum nanorods (Figure 1.1 (a)-(c)).
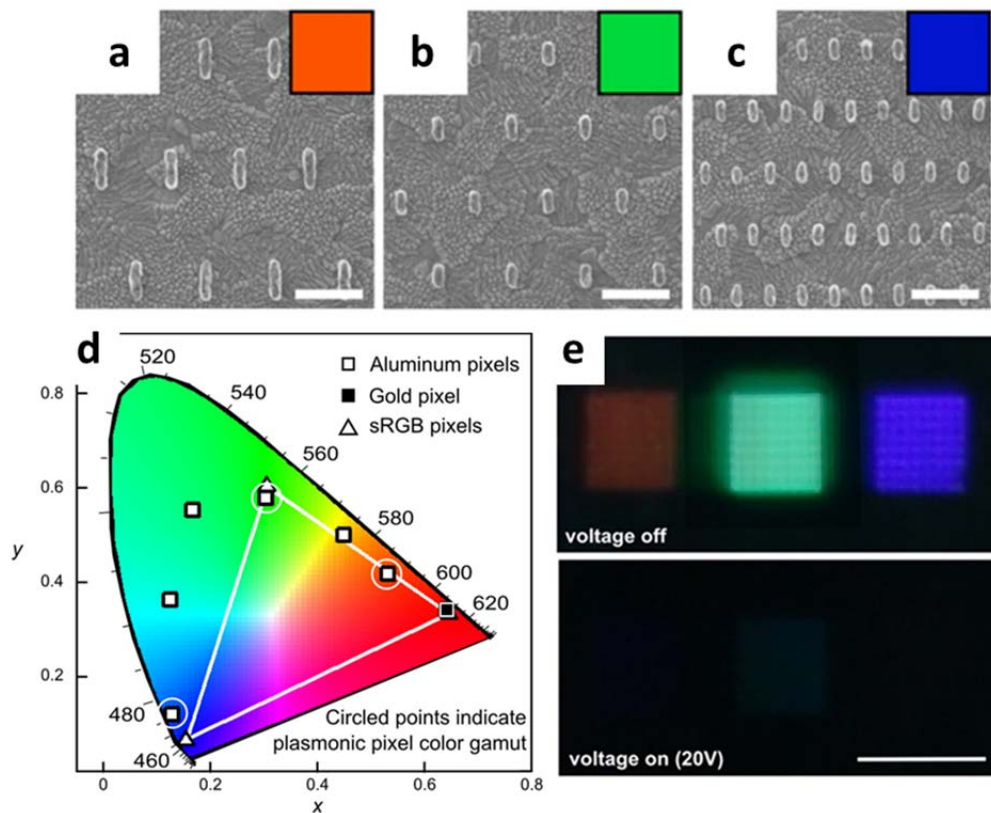
Figure 1.1 – Alumium Plasmonic Pixel in LCD device. SEM images of the red, green and blue plasmonic pixels are shown in (a), (b), and (c), respectively. The scale bar is 250nm long. (d) The colors of the aluminum and gold pixels are plotted on an CIE color diagram. (e) The three color pixels are truned on and off in an LCD device. The scale bar here is 2mm long.[3]

Based on the size and arrangement of the rods on the pixel surface, it will scatter a different color that can be plotted on an CIE diagram (d). In addition, the pixels were also incorporated in a liquid crystal layer, and could be turned on and off by applying a voltage (e).

1.1.2. Stretchable Plasmonics

Developing tunable nanophotonic devices based on elastic substrates has become an active research topic in recent years. One advantage of this approach is that mechanical deformation of photonic nanostructures fabricated on flexible substrates allows for simple, quick, and reproducible tuning of photonic devices.[17–20,23,34,35] In addition, PDMS is known to be elastic, inert, nontoxic, and nonflammable. Common applications include solar cells[36], iLEDs[37], tunable filters[38], hemispherical electronic eye cameras[39], and even metalenses[20]. One example for a stretchable plasmonic device is shown below in Figure 1.2 that was reported by Gao et al.[40] The array of gold nanoparticles has a resonance in the near IR at around 770nm in the unstretched state and is shifted to 1310nm with a total of 107% stretching. In addition, buckling was observed for larger stretching conditions.[40]
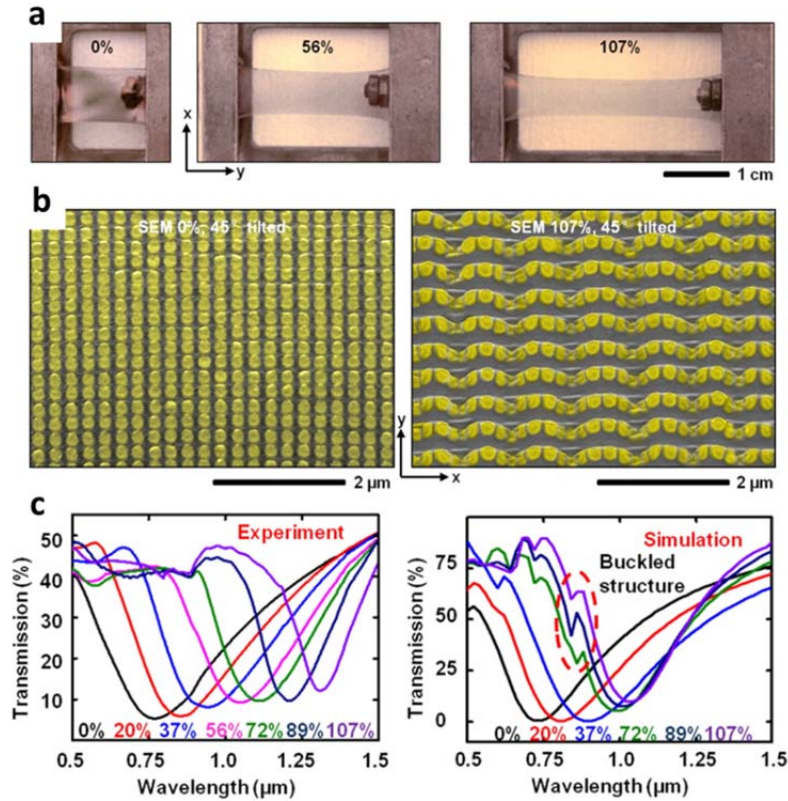
Figure 1.2 – Example of Stretchable Plasmonic Device. (a)Picture of the flexible silicone substrate and (b)SEM images of the gold nanostructures under different stretching conditions. (c)Experimental and simulated tranmission spectra that show the shift in resonance position with sample deformation. [40]

1.2. Device Design/Theory

The goal of this work is to combine the advantages of aluminum pixels and stretchable plasmonics to make a full-color stretchable plasmonic device. Even though there has been a verity of work in this area, current devices either only cover part of the visible spectrum[18,23,40–43], suffer from large resonance line widths[22,23], or report the device response in terms of extinction instead of scattering peaks[18,41,42].

Resonance tuning over large ranges from part of the visible to the near IR spectrum by extensive stretching in one direction has been reported as well[40–42]. This however can be limited by the elastic properties of the polymers. Passing the elastic limit can lead to hysteresis and cause deformation and degradation with repeated use[44,45].

In light of this, a two-dimensional stretching approach is implemented in this work, in order to achieve a full color tunable plasmonic device. It is composed of a two-dimensional periodic array of rectangular shaped aluminum nanostructures. To achieve full color tuning, the building blocks of the nanoparticle array should have a large scattering efficiency across the whole visible regime. The individual nanostructure was designed with a width of 100 nm and a length of 130nm (see inset of Figure 1.3(a)).
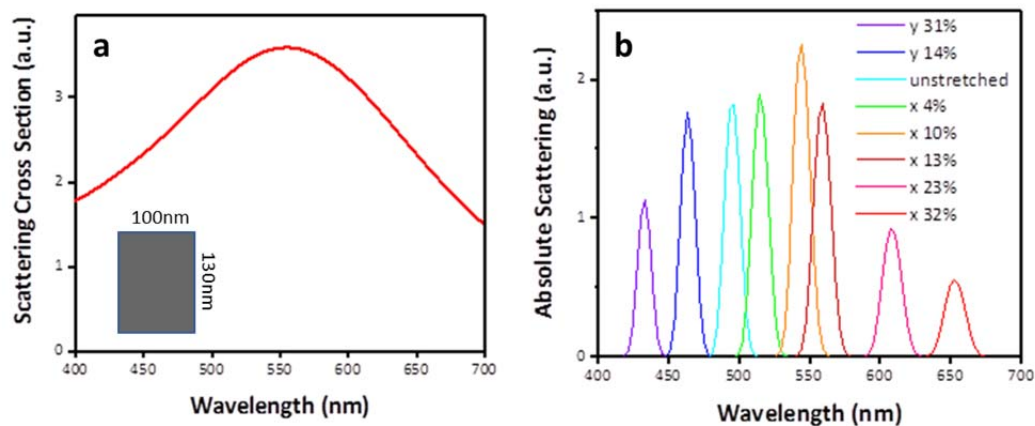
Figure 1.3 – Design Simulations. (a) The simulated scattering spectrum of an individual nanostructure is shown. The shape and dimensions are displayed in the inset. (b)The simulated scattering spectra of the plasmoinc device under different stretching conditions.

In this way, the single structure shows a broad scattering spectrum across the visible regime; centered at around 550nm (Figure 1.3(a).). However, when arranged into a two-dimensional array (Figure 1.4), the line width becomes substantially narrowed by far field diffraction. This allows for specific colors to be produced at the collection cone. In particular, when a lattice is formed light of different wavelengths forms a diffraction pattern governed by the diffraction formula:

$$\lambda = P_x n (\sin \theta_{incident} + \sin \theta_{observation})$$

Here, λ is the wavelength that constructively interferes at the observation angle $\theta_{observation}$. P_x is the period in the x-direction (see Figure 1.4), which is the lattice constant that is significant for diffraction in this case. n is the refractive index of the medium, and $\theta_{incident}$ is the incident angle.

The fundamental working principle is demonstrated in Figure 1.4. Only a specific wavelength window supports constructive interference within the collection cone, while the light for the rest of the spectrum is suppressed by destructive interference. The smaller the wavelength window is, the more vivid the observed color will be. To narrow the collection cone further, a beam stop was added to the objective used for light collection (see Figure 1.6). In terms of the two angles θ_{colmin} and θ_{colmax} (that are the minimum and maximum collection angles) the diffraction equations can now be written as:

$$\lambda_{max} = P_x n (\sin \theta_{incident} + \sin \theta_{colmax})$$

$$\lambda_{min} = P_x n(\sin\theta_{incident} + \sin\theta_{colmin})$$

$$\delta\lambda = P_x n(sin\theta_{colmax} - sin\theta_{colmin})$$

It can now be observed that the size of the wavelength detection window $\delta\lambda = \lambda_{max} - \lambda_{min}$ depends on both the collection cone $\theta_{colmax} - \theta_{colmin}$ and the lattice constant P_x. In this work, a narrow, fixed collection cone of 1.7deg was used, while the color was manipulated by changing the lattice constant P_x. This was achieved by transferring the aluminum nanostructurse on an elastic polymer substrate (for details see fabrication section). Physical stretching then allows for control over the lattice constant. In order to achieve full color tuning without approaching the elastic limit of the substrate, the device was designed to exhibit green light in its relaxed state (Figure 1.4(a)). When stretched along the long edge of the nanoparticles (y-axis), the lateral interparticle spacing along the x-axis is decreased due to material contraction, blue-shifting the scattering spectrum (b) Conversely, stretching along the short edge (x-axis) increases the lateral spacing between the nanostructures. The corresponding increase in the array period redshifts the peak position (c). Due to the strong restriction in the collection cone, the scattering color is highly sensitive to the lattice spacing and can in this way be tuned across the entire visible spectrum. Figure 1.3(b) shows the simulated far field spectra for this collection cone with different values for P_x, expressed as a percentage of stretching along the x or y axis. The two-dimensional stretching approach is an integral part in limiting the amount of overall strain required to achieve full-spectrum tuning. It can also be observed that the absolute scattering

intensities are dropping with increasing stretching condition (following the umbrella of the individual nanoparticle scattering), but remain of comparable order of magnitude.
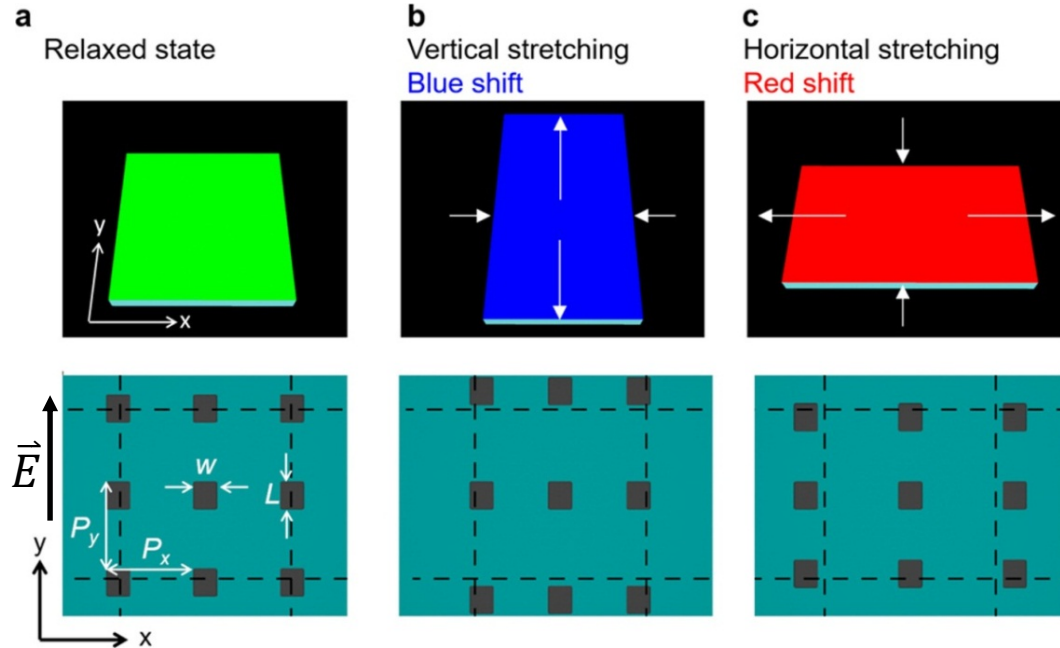
Figure 1.4 – Working principle of the full-spectrum stretchable plasmonic device. Top: schematic of the color change of the device under different stretching conditions. Bottom: corresponding schematic of the two-dimensional nanoparticle array. (a) 2D array in its relaxed state; (b) when stretched along its y-axis, and (c) when stretched along its x-axis. $P_x=P_y=400nm$, W=100 nm, L=130 nm. The height of the Al nanostructures is 35 nm.

1.3. Experimental

1.3.1. Sample Fabrication

The plasmonic nanostructures were fabricated in a multistep process. Initially, the aluminum nanoparticles on bilayer dielectric pillars of hydrogen

silsesquioxane (HSQ) and poly(methyl methacrylate) (PMMA) were fabricated on an n-type silicon substrate. This was achieved by using electron beam lithography, followed by development, oxygen plasma etching, and aluminum evaporation. In The array size was 50μm $\times$ 50μm. The arrays were subsequently transferred to a low-modulus, adhesive PDMS substrate (Figure 1.5(a)). A top-view scanning electron microscope (SEM) image of the as-fabricated aluminum nanoparticle/HSQ/PMMA multilayered structure is shown in (b). An SEM image of the silicon substrate after PDMS curing and stripping is shown in (c), confirming that the aluminum nanoparticles have been transferred to the PDMS substrate.

In the following I will describe the individual fabrication steps in detail. First, layers of PMMA 950 A2 resist (thickness~70 nm) and HSQ (DOW CORNING, XR-1541-002, thickness~70 nm) were spin-coated on an n-type silicon substrate (resistivity: 0.01~0.02 Ωcm), and baked at 250 °C for 2 mins. Then, an e-spacer layer was coated on the sample before e-beam exposure to make the surface conductive. Next, electron beam pattering was performed using an e-beam lithography system (FEI Quanta 650) at an acceleration voltage of 30keV with a beam current of 40pA. After e-beam exposure, the e-spacer was washed away again with deionized water, and the sample was developed by immersing the substrate in a 2.3% TMAH (MF-319) solution at room temperature for 70s. Oxygen plasma etching (Fischione, 660W) was subsequently performed for 73s to directionally etch the PMMA layer.
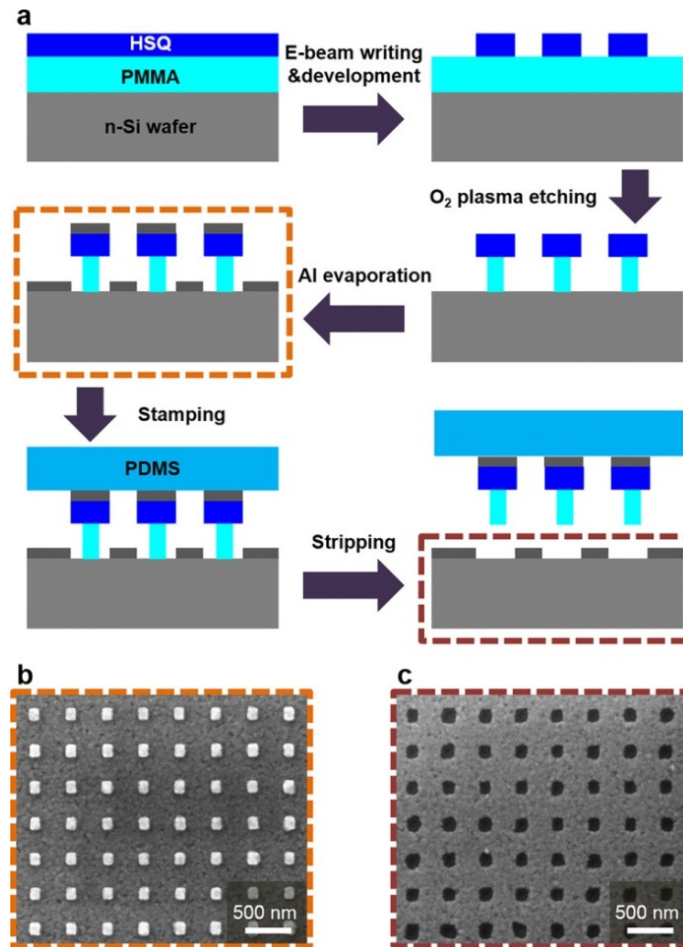
Figure 1.5 – Fabrication of the full-spectrum stretchable plasmonic device. (a) Schematic of the sample fabrication process. E-beam lithography was performed on the HSQ/PMMA layer on the n-Si substrate, followed by development, oxygen plasma etching and Al evaporation. The nanostructures sitting atop the HSQ/PMMA pillars were then transferred to the PDMS. SEM images of the Al-coated Si template (b) before and (c) after PDMS stripping.

Then, aluminum nanoparticles sitting on the HSQ/PMMA pillars were made by e-beam evaporation of a 35nm layer of aluminum (base pressure: 5×10^{-7} Torr, evaporation rate: 0.1nm/s).To make the elastic PDMS substrate the weighing base and curing agent of a commercial material (Sylgard 184, Dow Corning) were mixed with a ratio of 35:1. The solution was then degassed and cured at room temperature

and at 80°C for 12 and 2 hours, respectively. The thickness of the produced PDMS was around 2mm. To transfer the aluminum nanoparticles from the silicon to the PDMS substrate, the donor was first stamped onto, and then stripped from the PDMS. Due to the good adhesion between aluminum and silicon, only the aluminum nanoparticles, which are sitting on HSQ/PMMA pillars (poor adhesion to silicon), can be transferred to the PDMS.

1.3.2. Spectral Measurements

The scattering spectra of the plasmonic device for a range of stretching ratios were measured using a hyperspectral dark-field microscopy setup (Figure 1.6).
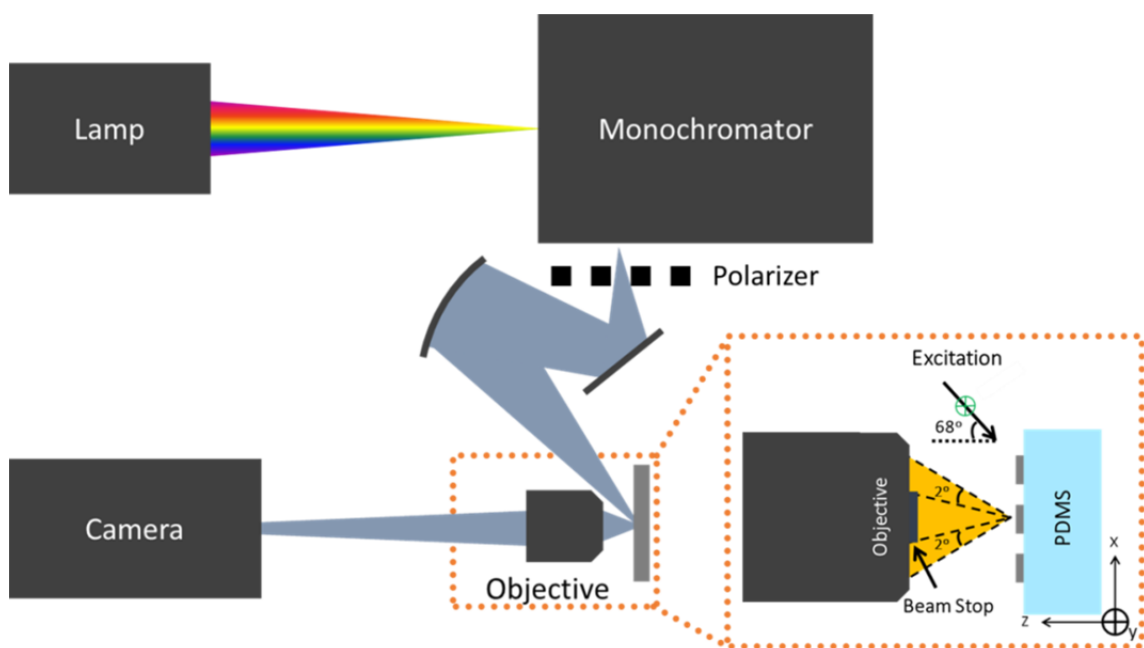
Figure 1.6 – Schematic of the hyperspectral dark-field microscopy setup.

A continuum laser driven light source (Energetic LDLS) was used in combination with a broadband polarizer (s-polarization) and a 1200 g/mm scanning monochromator (Princeton Instruments Acton SP2150) to produce the excitation beam. It was weakly focused onto the sample at an incident angle of 68°. The scattered rays were then collected via a reflective objective (Edmunds Optics, 15X/0.28). A beam stop was added to restrict the collection cone from 17.4^o to 19.1^o. The objective then focused the light onto a CCD (Princeton Instruments PIXIS 1024) for detection. To minimize noise the camera was cooled to -70° C. Using this method, monochromatic images between 400 and 700nm were obtained. The wavelength increments for the spectral scans were 5nm. Finally, the scattering spectra were calculated by subtracting the sample's scattering response from the substrate background and dividing by a white calibration to correct for the light source spectrum.

1.4. Discussion

CCD images, normalized experimental and simulated scattering spectra under different stretching conditions are shown in Figures 1.7(a), (b), and (d), respectively. Overall, the experimental and simulated spectra are in good agreement. The small variations between the observed and the simulated spectra could be due to sample imperfections or minor surface buckling[40]. All scattering spectra show very sharp profiles with a full width at half maximum of less than 20 nm. As the strain was increased from 0% to 32% along the short axis of the array, the scattering peak was red-shifted from 495nm to 645nm. Conversely, the peak

wavelength was shifted to nominally 440nm by stretching the device up to 31% along the long axis of the nanoparticles. The peak position blue-shifts only about half as far as it red-shifts for comparable stretching in the two respective directions. This is because horizontal contraction is nonlinear with respect to vertical expansion.
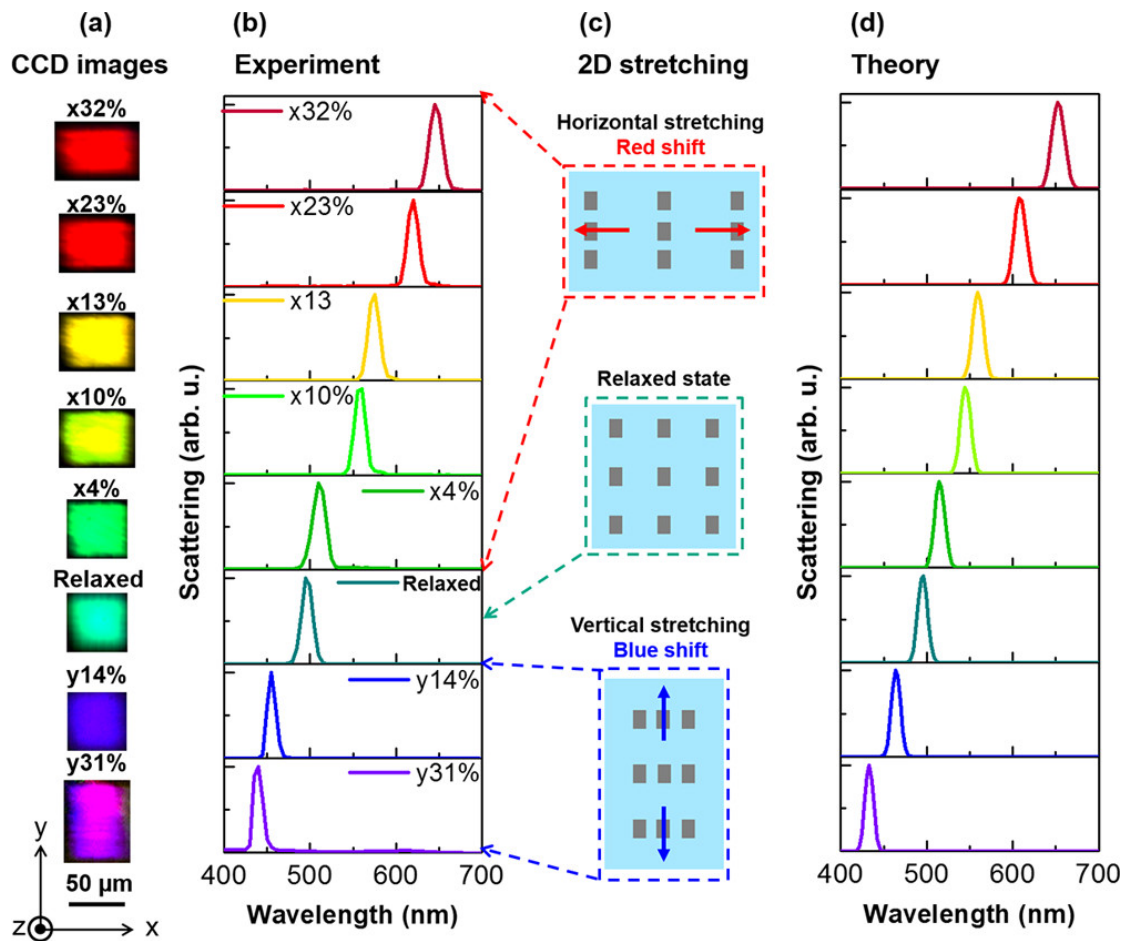
Figure 1.7 – Full color tuning on a single plasmonic device. (a) CCD images and (b) normalized experimental spectra of the device at different stretching conditions. Note that the axes in (a) are the same as the ones in Figure 1.6. (c) Schematic of the two-dimensional stretching method for full-color tuning. (d) The corresponding normalized simulated scattering spectra.

With both effects combined, the scattering window of the plasmonic device was tuned across the visible spectrum while keeping the maximum strain at less than 35%. All strains are well below the elastic limit for most PDMS fabrication protocols The stress-stain relationship in PDMS strongly depends both on the mixing ratio of base to curing agent[44,45] and the curing temperature[46]. One can define an elastic limit beyond which the material starts to show hysteresis. For common mixing ratios, this limit falls between 50-100% of strain. A higher ratio of base to curing agent will lead to a lower Young's Modulus and therefore a higher elastic limit. Kim et al.[44] have reported an elastic limit of around 100% for a mixing ratio of 15:1. The ratio used in this work was around 35:1, and it can therefore be safely assumed that the elastic limit is at least this high. Since the maximum strain was no larger than 35%, we are confident that all the strains used here fall far below the elastic limit. In this context, two-dimensional stretching is very useful for our PDMS-based device. With this method, full color tuning can be achieved without heavily stretching (i.e., beyond the linear regime of the deformation of PDMS) the substrate. It not only prevents device damage during the stretching process, but also improves the repeatability. The smallest increment in which we could repeatedly tune the device was about 0.5mm. This corresponds to about 4% strain. However, to more accurately determine the amount of stretch for any given measurement, we compared the sample dimensions in the optical images in the relaxed and the stretched state.

In order to test the repeatability of our device, we stretched it in multiple intervals up to one hundred times (Figure 1.8). The peak position varies only

slightly (up to 15nm), which is most likely due to inaccuracy in returning to exactly the same stretching condition each time. We did not observe any material distortion within the stretching cycles reported in Figure 1.8.
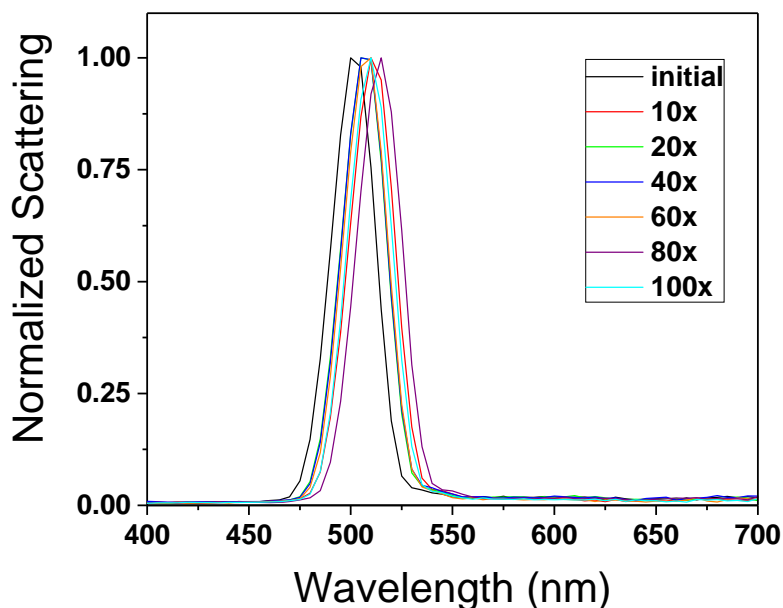
Figure 1.8 – Repeatability Test. The peak positions only shift slightly with repeated measurments.

The chromaticity, or color purity, corresponding to the spectrum of the plasmonic device at different stretching ratios was analyzed by convolving each spectrum with the Commission internationale de l'éclairage (CIE) 1931 color matching functions. The calculated results are labeled on the CIE 1931 chromaticity diagram shown in Figure 1.9. The white triangle plotted on the chromaticity diagram corresponds to the limit of the standard red–green–blue (sRGB) color gamut. Notably, all the colors fall outside of this triangle, indicating that the plasmonic device can produce much more vivid colors than

the sRGB color gamut. The area of the CIE color diagram covered by connecting the points from the plasmonic device is approximately 76%. To the best of our knowledge, this is the largest value reported for any tunable plasmonic device.
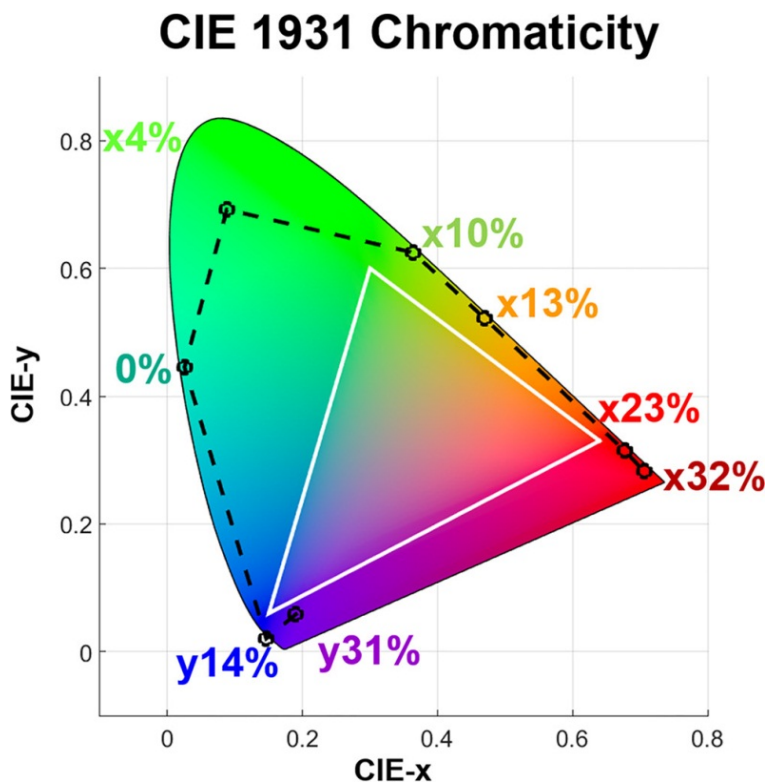
Figure 1.9 – Full color tuning. CIE 1931 chromaticity diagram overlaid with the sRGB gamut (white line). Device colors with different stretching ratios are shown as well. Here x and y are the standard color coordinates.

According to FDTD simulation results, at the scattering peak, around 5.6% of the source energy at that wavelength was collected by our detector. To improve this efficiency, the unit cell could be replaced with a more complex nanostructure (e.g., metal/insulator/metal multilayered nanoantenna[35]) to enhance the interaction between the device and incident light. In fact, there are two ways of defining a

scattering efficiency for our device: one is an evaluation of the ratio between the scattered signal intensity and the source intensity at the peak wavelength (peak efficiency), while the other is the ratio obtained by integrating over the whole visible spectrum (whole-spectrum efficiency). While the peak efficiency remains roughly constant for different collection cones, the whole-spectrum efficiency is lower than the peak efficiency, but it gradually increases as the collection angle increases. For example, for the 1.7degrees that was used in this work the whole spectrum efficiency was calculated to be 0.34%. Simulations show that it can be increased to 1.93% for a collection cone of 14.1 degrees. However, in that case the monochromaticity becomes worse (not all points fall outside of the sRGB triangle), and an additional horizontal point (50% stretch) has to be included to cover all desired wavelengths.

1.5. Dynamic Pattern Switching

To further show the potential of this device, dynamic switching between devices was demonstrated. Even though the erasing and restoring of an optical image consisting of plasmonic pixels has recently been reported[8], continuous switching of optical images through mechanical deformation has not yet been achieved. In addition to full color tuning, dynamic, image switching can also be realized with our stretchable plasmonics device. The working principle of the image switching is illustrated in Fig. 1.10(a). The device contains patterns which consist of plasmonic nanoparticle arrays with different periods. When illuminated with a white light source, the patterns scatter different colors due to their differing

periodicities. However, when the wavelength window of the incident light is narrow,

only the pattern containing the array with the matching period can be observed.
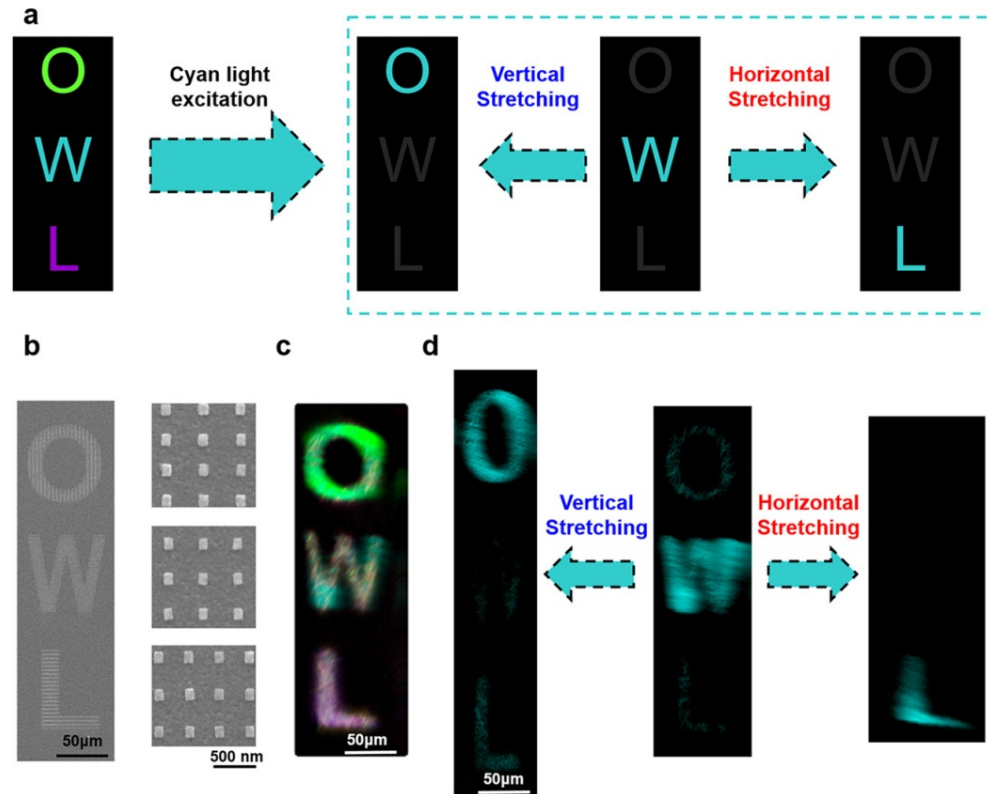
Figure 1.10 – Dynamic image switching. (a) Schematic of image switching based on stretchable plasmonic patterns. (b) SEM images of as-fabricated patterns (O, W, L) before they were transferred onto the PDMS substrate. Magnified SEM images of the respective patterns are shown in the right panel. (c) CCD image of the plasmonic patterns under white light illumination. (d) Dynamic, multilevel image switching between dark field images scattered from plasmonic patterns under different stretching conditions.

To demonstrate this, three adjacent patterns of the letters O, W, and L, with

different periods were fabricated and transferred onto a PDMS substrate. SEM

images of these three patterns prior to transfer are shown in (b). The patterns (O,

W, L) with corresponding periods (x, y) = (429nm, 348nm), (400nm, 400nm), and (348nm, 429nm) lead to different scattering peak positions at 430nm, 495nm, and 530nm, respectively, for the device in its relaxed state. When the patterns are illuminated with a white light source, the colors of the letters O, W, and L are purple, cyan, and green, respectively (c). As shown in the middle panel of (d), when cyan light with a wavelength window of 465-505 nm is used as an excitation source, only pattern W can be observed clearly in the relaxed sample, because it is the only one pattern with its scattering peak located in this excitation window. When stretching the whole device horizontally by 15%, all the scattering peaks of the three patterns are red-shifted. Now, only pattern L can be observed clearly in the dark-field image, since the scattering peaks of the other two patterns are both beyond the wavelength window of the incident light. Similarly, only pattern O can be observed clearly when the sample is stretched vertically by 26% (d). For an excitation wavelength of 490nm, the ratio of the maximum scattering intensity of the bright letter to the two dark letters under different stretching conditions is 9.6, 9.1, and 29.7 for the cases of O, W, and L, respectively. Even though we have restricted the number of images to three in this case, in principle this number could be greatly increased. By judicial choice of pattern period, switching between many different images should be possible. The narrow linewidth of the peaks allows for switching between devices of many different periodicities.

1.6. Conclusion

In conclusion, I have presented a stretchable plasmonic device that can achieve both full-spectrum tuning as well as active, multiple image switching. The sharp scattering spectra of the 2D aluminum nanostructure arrays yield highly vivid colors that can be easily tuned across the visible spectrum. Furthermore, active switching between multiple optical images is made possible. In both cases, two-dimensional stretching limits the amount of elastic strain required for these effects to less than 35%. This is ideal for integration into compact microelectromechanical systems (MEMS) based photonic devices. Overall, this full-spectrum plasmonic device has a wide and diverse range of possible applications, such as highly sensitive surface stress or colorimetric sensors, ultra-compact MEMS-based spectrometers, active color filters, as well as new types of real-time displays.

Chapter 2

ZnO Metamaterial for Deep UV SHG

The work presented in this chapter has not been published yet. Similarly to the first chapter, it is based on a collaboration between Dr. Ming-Lun Tseng, Jian Yang, and myself. I was working under the supervisor of my advisor Dr. Naomi Halas. Dr. Ming-Lun Tseng was supervised by both Dr. Naomi Halas and Dr. Din Ping Tsai. All simulations were performed by Jian Yang and Ming Zhang. Both were working under the supervision of Dr. Peter Nordlander. Dr. Ming-Lun Tseng and I worked on the experimental part together. However, due to considerations of highest efficiency, Dr. Ming-Lun Tseng performed the Focused Ion Beam (FIB) fabrication at the Research Center for Applied Sciences (RCAS), Academia Sinica in Taiwan (under the supervision of Dr. Din Ping Tsai), while I focused on the linear and nonlinear measurements and the related data analysis.

Nonlinear optical processes have become important for many different applications. Besides nonlinear crystals, novel metamaterials that allow for

immense control over the nonlinear wave front have become popular. So far, the most common nonlinear processes for metamaterials remain near IR to visible light conversion. To the best of my knowledge, deep ultraviolet (DUV) generation with nonlinear metamaterials has not been achieved yet. However, this wavelength regime (200-280nm) has many interesting applications[47]. In the following I will present first results on an all-dielectric ZnO metamaterial for second harmonic generation, starting with a pump wavelength of 394nm and generating the second harmonic which falls right at the edge between the DUV and the Vacuum UV (VUV) which is the wavelength regime between 100 and 200nm. The work was motivated by the difficulty of generating and controlling DUV and VUV light. Nonlinear, all-dielectric metamaterials are a promising alternative to special UV crystals.

2.1. Nonlinear Optics Introduction

The following introduction to Nonlinear Optics (section 2.1) includes general concepts that were researched in the following textbooks: 'Fundamentals of Photonics', Chapter 21 by Saleh B. and Teich M.[48], 'Nonlinear Optics' by Boyd R.[49], and the Handbook of Laser Technology and Applications, Chapter C3.1 that was written by David J Binks[50].

Traditionally, it was believed that the relation between the electric field in a material and the induced polarization was linear for all materials. While this is certainly true at low powers, it does not hold when the electric field strengths become comparable to interatomic fields, which occurs at around 10^5-10^8 V/m. At

these field strengths the optical material properties are changed by the extreme fields and cause new fields that can in turn interact with the original field. This power dependence of the optical material properties stands at the core of nonlinear optical phenomena. The linear relation $\vec{P} = \varepsilon_0 \chi \vec{E}$, is now no longer valid and must be replaced by a nonlinear function that captures the power dependence of the induced polarization. For most light intensities, like the ones used here (around $1GW/cm^2$), the nonlinear effects are still comparably small, and allow for a Taylor expansion of the nonlinear polarization around $E = 0$. The nonlinear coefficients can then be defined as follows:

$$\vec{P} = \varepsilon_0(\chi \vec{E} + \chi^{(2)} \vec{E}^2 + \chi^{(3)} \vec{E}^3 + \cdots)$$

While the linear coefficient χ is a rank two tensor, it can be readily extrapolated that $\chi^{(2)}$ must be a tensor of rank three, $\chi^{(3)}$ of rank four, and so on. In an anisotropic material, there can be a preferred direction in which the nonlinear coefficient is largest. In the following, no explicit tensor notation will be used for simplicity.

To visualize nonlinear optical processes, a simple analogy to the harmonic oscillation of a mass on a spring can be considered. For small displacements, Hook's law applies and yields the mass displacement from equilibrium in a linear relation to the restoring force. However, if the displacement increases beyond the linear regime of the spring, nonlinear terms have to be added to Hook's law to compensate for the altered material properties. The motion is now no longer simple harmonic but can be described as an anharmonic oscillator. The consequences of the

nonlinearity are dramatic. First, the refractive index of a material is no longer a constant, but power dependent. Second, as will be extensively used in this thesis, light can change frequency when it propagates through a medium. Finally, for completion it should also be mentioned that in nonlinear optics, the superposition principle is violated, and since the presence of photons can alter the dialectic environment, light can be used to control light[51].

2.1.1. Second Harmonic Generation

Second Harmonic Generation (SHG) is one of the simplest nonlinear processes in which two photons combine inside a nonlinear material to form a photon of twice the original energy. This was first observed as in 1961 by Franken et al. [52], shortly after the invention of the laser. To understand this process one can consider a material, in which the first term in the Taylor expansion is sufficient to describe the material nonlinearity. The fundamental equation is simply given by:

$$\vec{P} = \varepsilon_0(\chi\vec{E} + \chi^{(2)}\vec{E}^2) \equiv \vec{P}_L + \vec{P}_{NL} \ (1)$$

Where $\vec{P}_L$ and $\vec{P}_{NL}$ are defined as the linear and nonlinear polarization, for convenience. If now a plane wave with angular frequency ω, described by:

$$\vec{E}(\omega,t) = \vec{E}(\omega)e^{i\omega t} + \overrightarrow{E^*}(\omega)e^{-i\omega t} \ (2)$$

is incident on the nonlinear material, the incident field (2) can be substituted in to the definition of the nonlinear polarization (1) as:

$$\vec{P}_{NL}(\omega, t) = \varepsilon_0\chi^{(2)}[\vec{E}(\omega)^2 e^{2i\omega t} + \overrightarrow{E^*}(\omega)^2 e^{-2i\omega t} + 2|\vec{E}(\omega)|^2]$$

It is now convenient to separate the nonlinear polarization into a time dependent and a time independent term:

$$\vec{P}_{NL}(\omega, t) = \vec{P}_{NL,0}(\omega) + \vec{P}_{NL,2\omega}(\omega, t)$$

with

$$\vec{P}_{NL,0}(\omega) = \varepsilon_0 \chi^{(2)} |\vec{E}(\omega)|^2$$

and

$$\vec{P}_{NL,2\omega}(\omega, t) = \varepsilon_0 \chi^{(2)} [\vec{E}(\omega)^2 e^{2i\omega t} + \vec{E^*}(\omega)^2 e^{-2i\omega t}]$$

It can be observed that the time dependent component of the nonlinear polarization is oscillating with a frequency of 2ω. Therefore, it radiates light at the second harmonic (SH) frequency of the incoming light. In addition, the time independent component creates at DC field. This process is referred to as optical rectification. Another important observation that can be immediately made from the fundamental equation is that second harmonic generation is forbidden in centro-symmetric systems. In such a system if $\vec{E} \to -\vec{E}$ then $\vec{P} \to -\vec{P}$, by symmetry. Equation (1) then turns into:

$$-\vec{P} = -\varepsilon_0 \chi \vec{E} + \varepsilon_0 \chi^{(2)} \vec{E}^2 \ (3)$$

However, (1) and (3) can only be simultaneously true if $\chi^{(2)} = 0$.

As stated above, $\chi^{(2)}$ is in fact a rank 3 tensor that has 27 components. However, since for interacting electric fields $E_i E_j = E_j E_i$ (the order has no physical significance) the number of elements can be reduced to 18. The nonlinear polarization can then be written in matrix form as:

$$\vec{P}_{NL} = \begin{bmatrix} P_x(2\omega) \\ P_y(2\omega) \\ P_z(2\omega) \end{bmatrix} = \varepsilon_0 \chi^{(2)} \vec{E}^2 = 2\varepsilon_0 \begin{bmatrix} d_{11} & d_{12} & d_{13} & d_{14} & d_{15} & d_{16} \\ d_{21} & d_{22} & d_{23} & d_{24} & d_{25} & d_{26} \\ d_{31} & d_{32} & d_{33} & d_{34} & d_{35} & d_{36} \end{bmatrix} \begin{bmatrix} E_x(\omega)^2 \\ E_y(\omega)^2 \\ E_z(\omega)^2 \\ 2E_y(\omega)E_z(\omega) \\ 2E_x(\omega)E_z(\omega) \\ 2E_x(\omega)E_y(\omega) \end{bmatrix}$$

Each coefficient d has a first index were (1, 2, 3) stand for (x, y, z), respectively, and a second index (1, 2, 3, 4, 5, 6) that combines two dimensions as (xx, yy, zz, yz or zy, zx or xz, xy or yx), respectively. However, for any given material not all components are usually nonzero or independent. As discussed previously, any centro-symmetric geometry will lead to a nonlinear coefficient of zero. For example, sputtered zinc oxide thin films (the material used in this research) have a wurtzite crystal structure with five nonzero components, of which only three $(d_{15}, d_{31},$ and $d_{33})$ are independent[53]:

$$\chi^{(2)} = 2\varepsilon_0 \begin{bmatrix} 0 & 0 & 0 & 0 & d_{15} & 0 \\ 0 & 0 & 0 & d_{15} & 0 & 0 \\ d_{31} & d_{31} & d_{33} & 0 & 0 & 0 \end{bmatrix}$$

Besides SHG there are many more common nonlinear processes. For example, two photons with frequencies ω_1 and ω_2 can be combined in a nonlinear medium to generate the sum $\omega_1 + \omega_2$ or the difference $\omega_1 - \omega_2$ of the two basic frequencies. SHG can in fact be considered a degenerate case of sum frequency generation. Starting with three photons, more complicated processes like third harmonic generation and four-wave mixing can be achieved. However, since this thesis focuses on SHG, these processes will not be discussed any further.

2.1.2. High Harmonic Generation

Another way to exploit nonlinear properties of materials is called High Harmonic Generation (HHG). This effect occurs for extremely high peak power densities around 10-10,000 TW/cm^2 [54,55]. At this point the nonlinear coefficients can be so large that the Taylor expansion of the nonlinear polarization is no longer valid. The effect is usually observed in gases (e.g. Ar, Kr and Xe). The fields are so strong that they can almost ionize the atoms. When the field reverses, the electron accelerates back towards the nucleus and emits all the odd harmonics of the laser frequency, up to a certain threshold, at comparable intensities. For example, nonlinear generation in He was reported to an order of 297 in 1997 [56].In this way, Extreme UV (EUV), and even soft X-ray pulses can be generated. The mechanism is drastically different from the perturbative nonlinear optics that has been discussed so far, since in the former the nonlinear coefficients become weaker and weaker with increasing order. The field has attracted attention in attosecond physics, since the harmonic pulses can have attosecond pulse widths However, due to the requirement of ultrashort pules, and the need for gaseous elements, the applications of this process are limited. In 2008 Kim et al. have claimed to use plasmonics to enhance HHG[54], but this was refuted by Sivis et al. who attributed the effect to atomic line enhancement[57]. Later in 2016, Han et al. showed that HHG is possible in metal-sapphire nanostructures. They generated harmonics in the EUV and even soft X-ray spectrum from 45-110nm. The required field densities were only around 100GW/cm^2 [54]. However, even though this is a large improvement from the usually required 10 TW/cm^2, the power density requirements are still high (they used a

12fs pulsed laser), and the reported conversion efficiency for the dominant seventh harmonic is only 10^{-11} [58]. While HHG has the potential to generate very high energy and very short pulses, the goal of the work reported here is to produce a simple, inexpensive DUV light source. For this it is imperative to achieve a better conversion efficiency at a lower power density.

2.1.3. Nonlinear Crystals vs Nonlinear Metamaterials

The conventional way to generate nonlinear optical processes like SHG is with the use of nonlinear crystals. The most common materials include beta barium borate (BBO), potassium titanyl phosphate (KPT), and lithium triborate (LBO). Nonlinear crystals are popular, due to their high conversion efficiencies, especially when operated with pulsed lasers. Modern LBO crystals from Castech for example can achieve second harmonic conversion efficiencies of over 70%[59]. Using an extra-cavity KTP second harmonic crystals from Newlight Photonics report over 80% SHG efficiency[60]. This is possible with crystals, since many active layers can be used in sequence, as long as the absorption is low at both the fundamental and the harmonic frequency. However, due to the difference in refractive index, phase matching is required. This can for example be achieved with birefringence or periodic poling (quasi phase matching).

However, even though the high conversion efficiencies make nonlinear crystals very popular, they also have significant disadvantages. Firstly, they are often expensive because they have to be grown and cut in a particular way to support the desired wavelength and to achieve phase matching. When considering

UV wavelengths, one can define three general regimes between 100 and 400nm: UV-A or near UV (315-400nm), UV-B or mid UV (280-315nm), and UV-C (100-280nm). The last regime can be subdivided into the deep UV (200-280nm) and the vacuum UV (100-200nm). While the UV-A and UV-B can be efficiently generated with nonlinear crystals, it becomes more difficult in the deep and especially the vacuum UV regime to find crystals that support this wavelength range. When generating VUV light, special, exotic materials like $KBe_2BO_3F_2$(KBBF)[61], $RbBe_2(BO_3)F_2$(RBBF)[62], or $BaBe_2BO_3F_3$(BBBF)[63] have to be used. Another disadvantage of nonlinear crystals is the nontrivial usage. To achieve phase matching a certain orientation of the crystal with a certain incident angle is often necessary. Since the nonlinear signal is very sensitive to these conditions, considerable effort usually goes into aligning the crystal. Again, this problem is particularly prevalent for VUV harmonic generation. According to Newlight Photonics, KBBF for example, grows in a plate-like crystal structure, which makes cutting the crystal at the phase matching angle impractical[64]. Alternatively, a prism coupled device[64] can be used for phase matching. It has been shown that using this approach second harmonic generation from 400nm to 200nm can be achieved with a conversion efficiency of 15% with Watt level powers[61]. The authors of this work also demonstrated that there device can work down to 185nm, but with reduced conversion efficiency[61]. In summary, simple and efficient SHG to achieve VUV wavelengths still remains a challenge.

Nonlinear metamaterials provide another route to SHG besides crystals. Metamaterials, or artificial electromagnetic media, form a novel class of materials that are constructed from individual building blocks, called meta-atoms. These unit

cells are typically plasmonic, phonon-polaritonic, or dielectric nanostructures. Metamaterials have been of significant scientific interest recently, because of their ability to confine, control, and guide light at the nanoscale. They can be used to achieve many exotic phenomena, like negative, or zero refractive index. In addition, they are of interest for device applications including beam steering or meta-lenses.[26].

The strong light confinement of the nanostructures within metamaterials can lead to strong field enhancements. Due to the nonlinear power dependence of nonlinear processes, this redistribution of the electric field density can produce enhancements in the conversion efficiency. In addition, for a single layer metamaterial, the issue of phase matching between different layers is absent. In the past, plasmonic structures have been shown to be promising to enhance the nonlinear effects of materials[65]. However, recently all-dielectric metamaterials consisting of loss-less semiconductor building blocks like silicon[4,36,66–72] or germanium[73] have moved to the frontier of the field. Their most significant advantages over their plasmonic counterparts are their transparent nature that avoids heating which is inherent to lossy plasmonic particles,[26] as well as their larger active volumes[74]. In the following, I will present an-all dielectric ZnO Metamaterial for DUV SHG.

2.2. Fabrication

The different fabrication steps for the all-dielectric ZnO sample are described in Figure 2.1 below. As a ZnO source, a 150nm thin film on a soda lime substrate

(MTI Corporation) was used (a). The thin film is polycrystalline with (002) orientation. After the substrate was thoroughly cleaned; a 5nm chromium layer was deposited via e-beam evaporation (b), to make the surface conductive. In this way charging effects during electron or ion beam exposure can be avoided. The base pressure was less than 5×10^{-6} Torr. Next, the patterns were cut using a gallium ion beam of a Focused Ion Beam (FIB) system (FEI Helios 660 NanoLab).(c) A beam control software (NPGS, JC Nabity Lithography Systems) was used for precise control over the ion beam, which is essential for successful patterning. The beam current was 38pA, the acceleration voltage was 30kV, and the ion beam dose $17\mu C/cm^2$. Finally, a SEM image of the fabricated structure is shown in part (d).
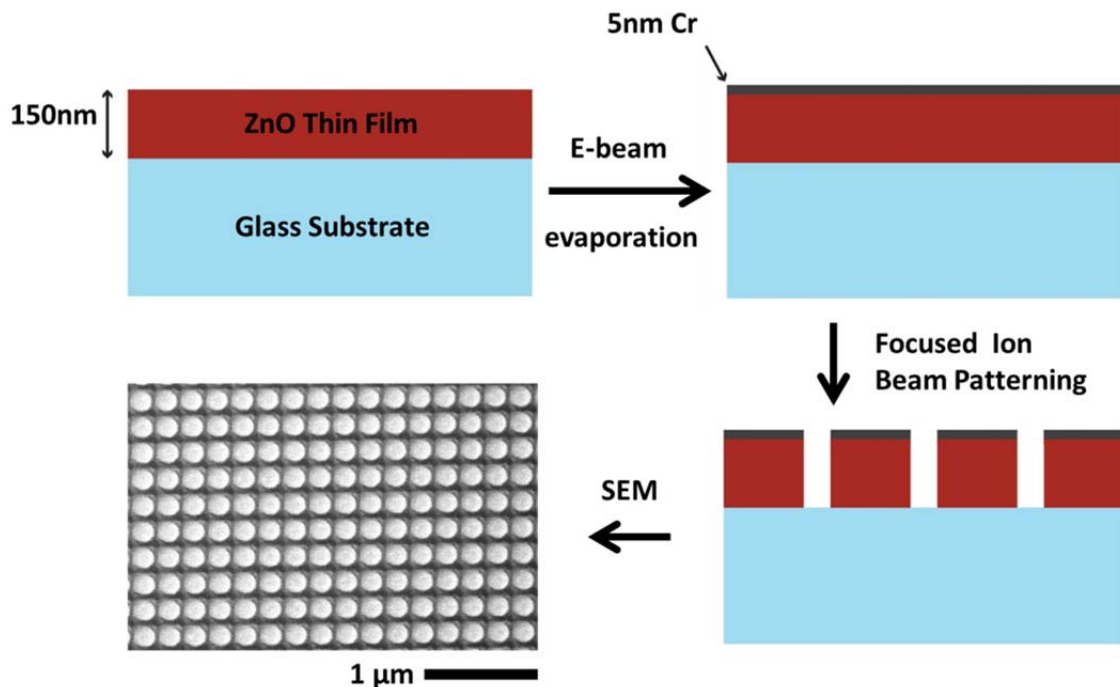
Figure 2.1 – Fabrication Method. (a)150nm ZnO thin film on a soda lime substrate. (b) 5nm chromium layer added for conductivity. (c) Patterning peformed via FIB. (d) SEM image of the patterned array.

2.3. Measurements

2.3.1. Linear

The linear spectra were taken with a transmission-based spectroscopy setup shown in Figure 2.2 below. The setup is mostly the same as the one for scattering described in Chapter 1, except that the light from exiting the monochromator was in this case focused on the sample with a 40mm UV fused silica lens, and collected in transmission.
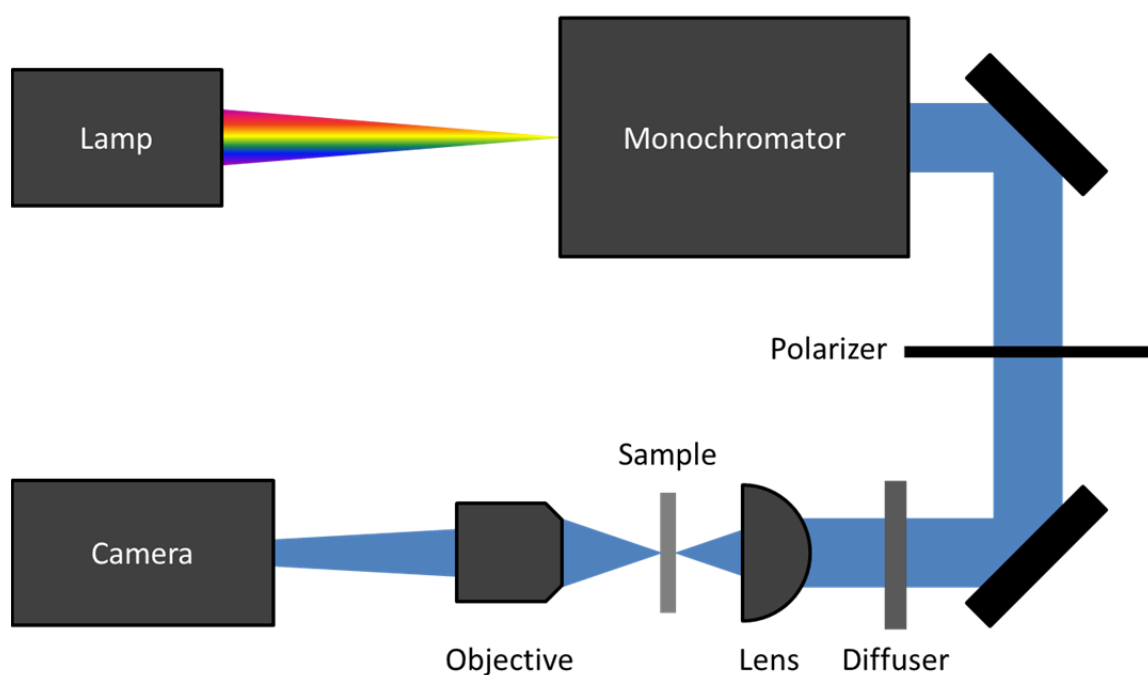
Figure 2.2 – Schematic of the transmission microscopy setup.

Also, a diffuser was added in this case to produce a more uniform beam The sample was oriented so that the light passed through the substrate first, and then

through the metamaterial. The relative transmission spectra shown in Figure 2.6(a) were achieved by dividing the signal from the sample by the one from the unpatterned ZnO substrate.

2.3.2. Nonlinear

The nonlinear measurements were performed using a mode locked, ultrafast Ti: sapphire laser setup (Figure 2.3). It consisted of a seed laser (Coherent Mira 900), and amplifier (Coherent RegA 9000) that together produced 205fs pulses with a repetition rate of 250kHz at around 788nm.
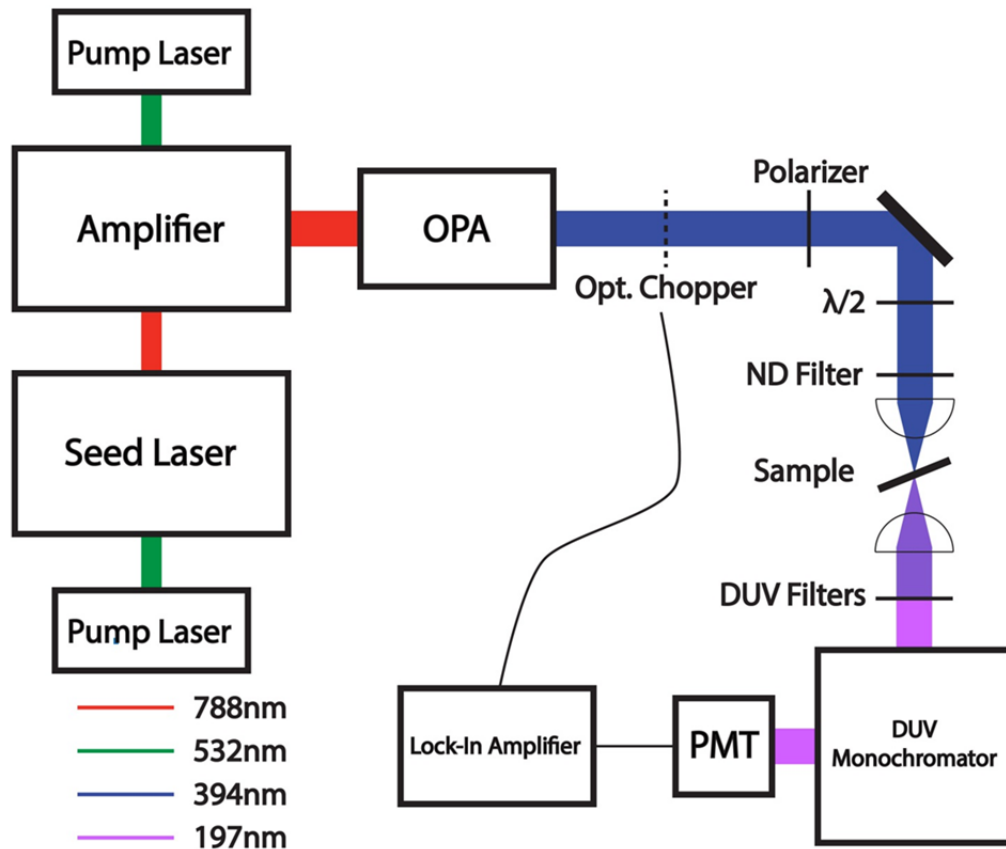
Figure 2.3 – Experimental SHG measurement setup for spectral scans.

Both were pumped by Coherent Verdi 5W, pump lasers. To generate the second harmonic an optical parametric amplifier (OPA) was used (Coherent OPA 9400). The produced 394nm beam was focused onto the sample with a UV fused silica lens (40mm focal length). Similar to the linear measurements, the light pump laser passed through the substrate first. This is important, because if the laser passed through the metamaterial first, the transmitted SH signal would be absorbed in the soda lime substrate and could not be observed in transmission. The incident peak power density on the sample ranged between 0.3 and 15GW/cm^2 with a spot size of about 227μm^2 (8.5μm beam waist radius). The peak power density was estimated based on the spot size, the pulse width and repetition rate of the laser. The transmitted linear and nonlinear signals were then collected with two CaF$_2$ lenses (40mm focal length each). The expected second harmonic wavelength was 197nm. For the spectral scans the light was then guided to the deep UV Monochromator (Thermo Jarrell Ash, 2400 groves/mm grating). The wavelength step for the spectral scans was 0.2nm. (However, only the scan in Figure 2.8 (a) was performed with a thin enough exit slit to resolve the spectral bandwidth). Two 200nm bandpass filters were used to reduce the linear signal. After the monochromator, the deep UV light was detected with a PMT (ADIT Electron Tubes, 9781B6019). It was chilled to around -14°C to minimize the dark current. To further increase the signal to noise ratio, the current signal from the PMT was fed into a lock-in amplifier (Stanford Research Systems SR850 DSP). Its reference frequency was provided by an optical chopper, which was placed in the laser path. The modulation frequency was 2.2kHz.

For all non-spectral measurements, including power and angle scans (change in incident angle ϕ, measured from normal), a simplified measurement setup was used (Figure 2.4). Three DUV filters were used to separate out the SH signal instead of using a monochromator. The PMT was a Thorlabs PMTSS in this case. This simplified setup only used minimal optics which is not only convenient in operation, but has the additional advantage that the attenuation of the SH signal by the optical components can be easily adjusted for in calculations, making it possible to accurately determine the conversion efficiency. In addition, a shorter path length also helps minimizes absorption of the SH signal in air. To compensate for any remaining fundamental signal, measurements with a glass slide (which acts as a long pass filter that blocks the SH signal) were performed, and subtracted proportionally.
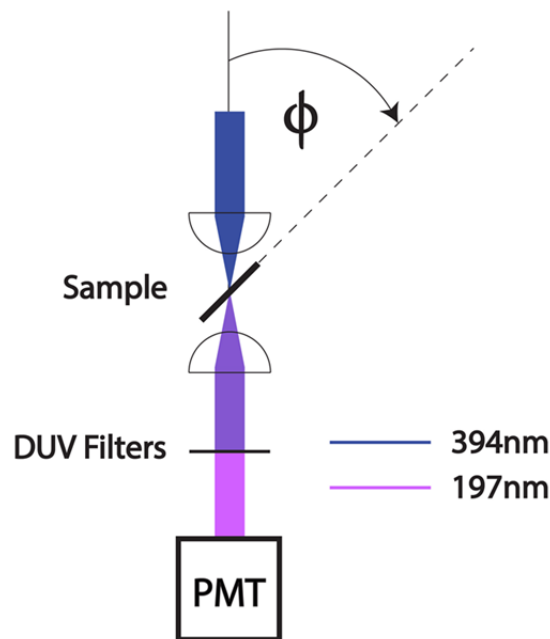
Figure 2.4 – Simplified SHG measurement setup for non spectral scans.

2.4. Discussion/Results

2.4.1. Sample Characterization

The all-dielectric metamaterial I am presenting here consists of ZnO nanodisks. It was designed to have a magnetic dipole resonance around 400nm. Figure 2.5 (a) below shows a schematic of the ZnO nanodisks used to construct the metamaterial. The diameter of the disks was about 175nm, and the periods were 222nm and 236nm in the x and z direction, respectively. This was determined from an SEM image of the sample. A schematic of the patterned metamaterial can be found in (b). The total array size was 20x20μm. An SEM image of the fabricated structure is shown in (c).
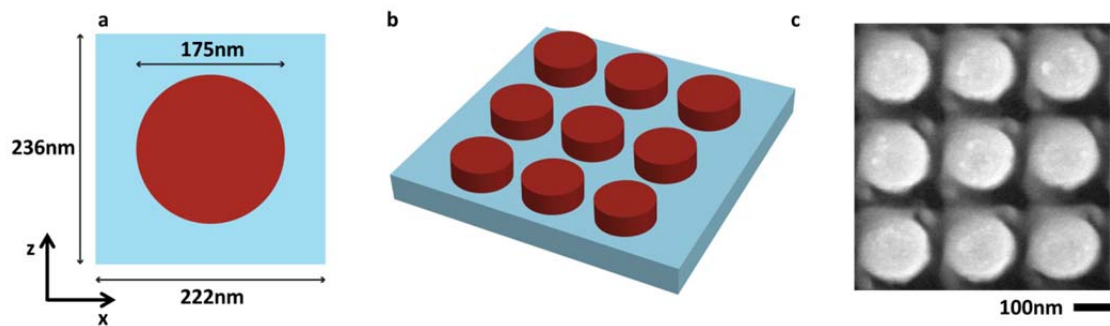
Figure 2.5 – Magnetic dipole sample. – (a) Scematic of the individual nanodisk with diameter of 175nm and (b) the metamaterial with periods P_x=222nm and P_z=236nm. (c) SEM image of part of the array.

Next, the linear response was analyzed. The experimental (a) and simulated (b) transmission spectra in Figure 2.6 show a resonance mode at around the fundamental wavelength. In order to make the simulations as accurate as possible

the actual disk diameters were measured from an SEM image, and a diameter of 173.5nm was used. The experimentally determined resonance is broader and slightly blue shifted compared to the simulated results. However, the resonance position was also predicted to depend on the incident angle, which allows for some manipulation. This will be discussed further in the next section
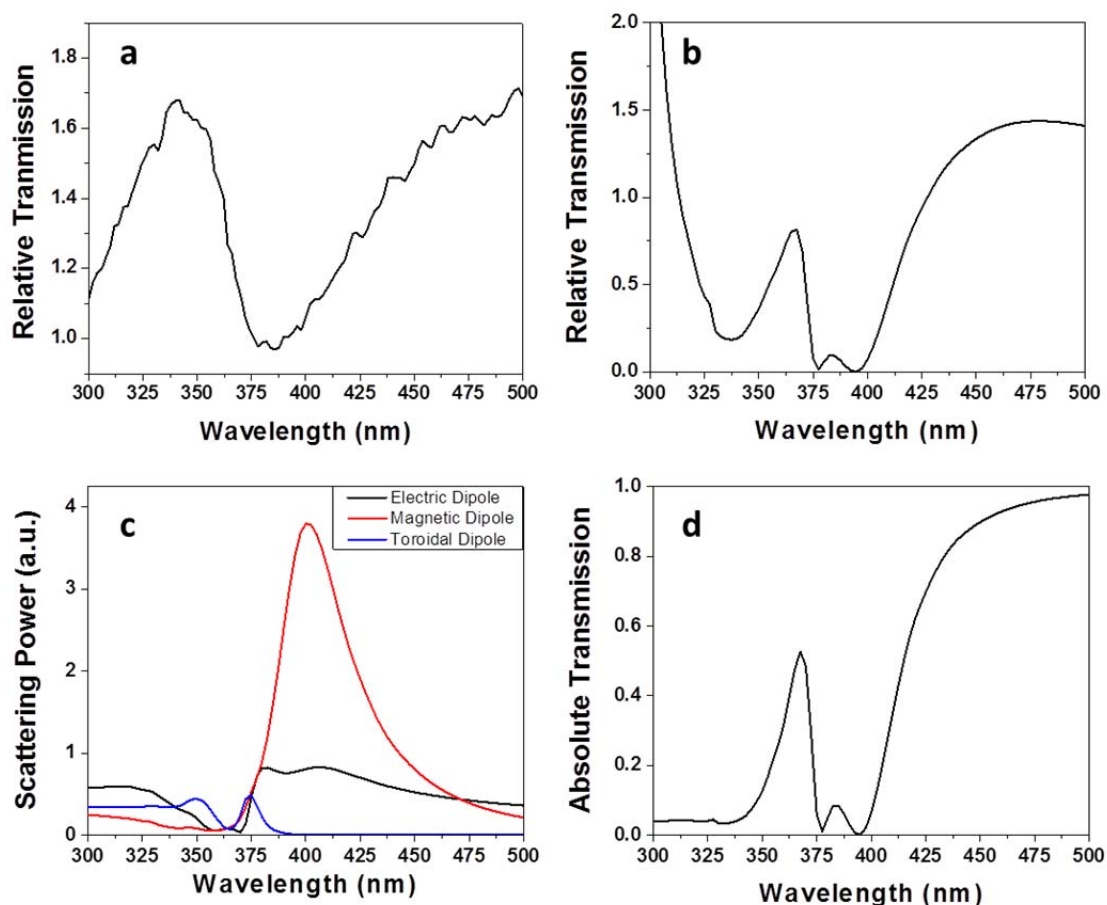
Figure 2.6 – Mode analysis. (a) Simulated and (b) experimental tranmission spectra. (c) Scattering power of magnetic and electric diple modes. (d)Simulated absoulte transmission.

The mode analysis (c) shows that the dip around 400nm is due to a magnetic dipole resonance. This type of resonance has been observed in dielectric nanoparticles before[26,72]. It occurs here due to the phase difference between the bottom and the top part of the disks that leads to a rotating electric field with alternating directions, and therefore a magnetic dipole. The second, bluer dip around 378nm can be attributed to an anapole mode; an interference between a toroidal and electric dipole mode[75]. However, in experiment we either do not observe this mode, or it is merged with the magnetic dipole mode. This could be due to imperfections in sample fabrication. Lastly, experimentally the relative transmission was measured with respect to the unpatterned thin film. However, the simulation in (d) indicates that the absolute transmission spectrum of the whole device is not much different with exception of the low wavelength end. This is because the soda lime substrate strongly absorbs in this wavelength regime. In experiment, most light in this regime is absorbed by the substrate. Therefore, even for relative transmission, noise dominates, and the ratio approaches one. All the above simulations were performed with COMSOL Multiphysics. Figure 2.7 shows field profile simulations of the electric (a) and magnetic (b) field distributions in the metamaterial. The rotating electric field is in the plane of the screen in (a) and perpendicular to the plane in (b), while the magnetic dipole is perpendicular to the plane of the screen in (c) and in the plane in (d).
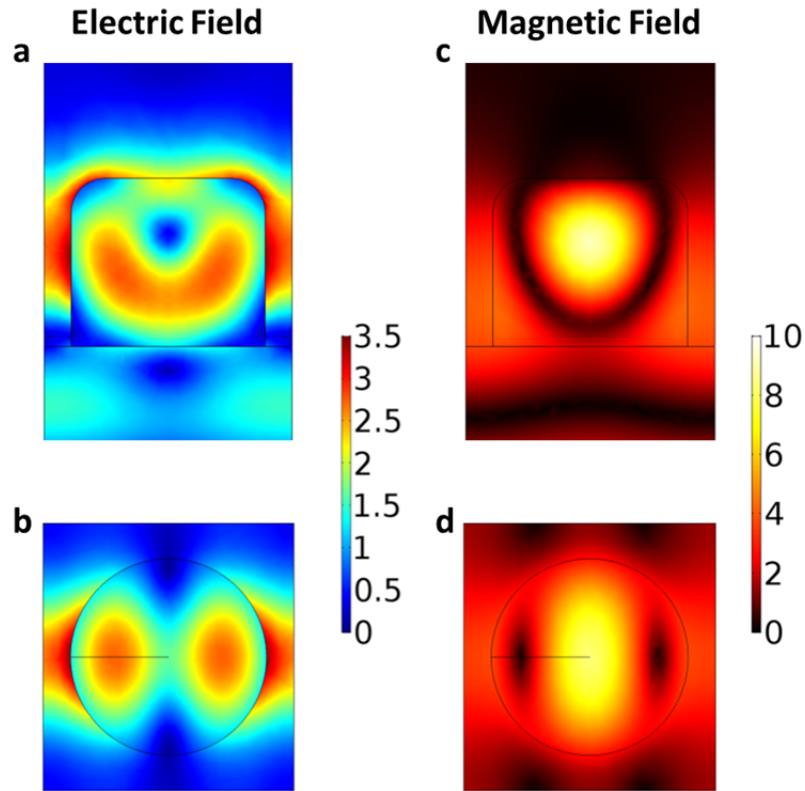
Figure 2.7 – Field profile simulations for a unit cell of the metamaterial. (a) Electric field profile in the side and (b) top view. (c) Magnetic field profile in the side and (d) top view.

The plots show a magnetic hot spot in the center of the disk and an enhancement of the electric field in a large volume on the inside and outside of the disks with a maximum field enhancement of around 3.5. Since SHG enhancement is proportional to the fourth power of field enhancement; this effect can cause significant changes in the SHG strength.

2.4.2. Second Harmonic Generation

Figure 2.8 (a) shows the spectrum between 193 and 202nm for the all dielectric ZnO metamaterial. A sharp peak can be observed at 197.6-198nm for p-polarized light. This wavelength falls right around the edge between the DUV and VUV regime. I will be referring to it as DUV signal, to avoid confusion. At this point, it is not clear to us yet if the SH response is due to the bulk or surface nonlinearity of ZnO. Further investigation on this is currently ongoing. However, (b) shows that p-polarization gives a significantly stronger signal than s-polarization.
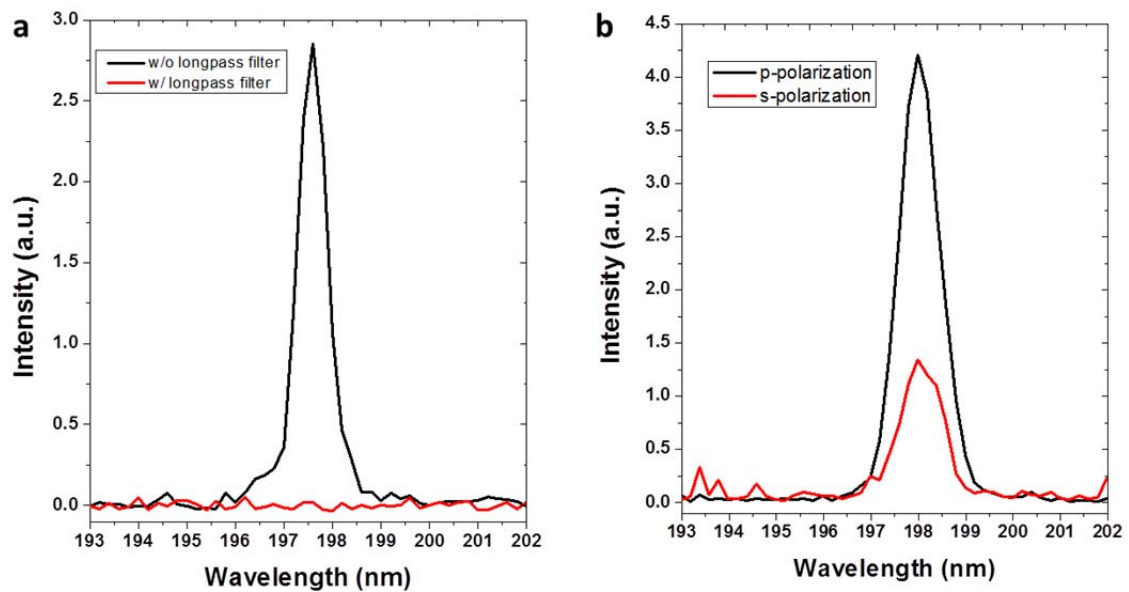
Figure 2.8 – Second harmonic signal of the magnetic dipole strucutre. (a)With and without a longpass filter, and (b) comparison between p- and s-polarization

The incident angle ϕ used here is 7deg (measured from normal). A more detailed discussion of the angle dependence is shown in Figure 2.9.

The measured fundamental wavelength was 394nm, so the expected wavelength was if fact 197nm. The small mismatch could be due to experimental inaccuracy or be explained by the bandwidth of the fundamental pulse (around 2.4nm). To verify that the measured signal is indeed due to the SH signal of the fundamental, two additional tests were performed. First, the same scan was performed with a simple glass slide in the detection path. It acts as a long pass filter and absorbs the DUV light. As Figure 2.8 (a) also shows, the nonlinear signal cannot be observed with the glass slide, indicating that the peak is indeed due to the DUV light. Second, power scans were performed (Figure 2.10).

Furthermore, the SH signal from the magnetic dipole structure was found to be strongly dependent on the incident angle ϕ (Figure 2.9 (a)). A maximum can be observed at 7deg. Part (b) shows a simulation of the overlap integral between the nonlinear polarization (which depends on the square of the electric field at the fundamental wavelength) and the electric field at the second harmonic wavelength. This integral predicts the strength of the nonlinear signal. This technique was adopted from O'Brien et al.[76] Bulk nonlinearity was assumed for these simulations, since it more closely resembled the experimentally observed behavior than the simulations based on surface nonlinearity. However, as mentioned more work is required here.
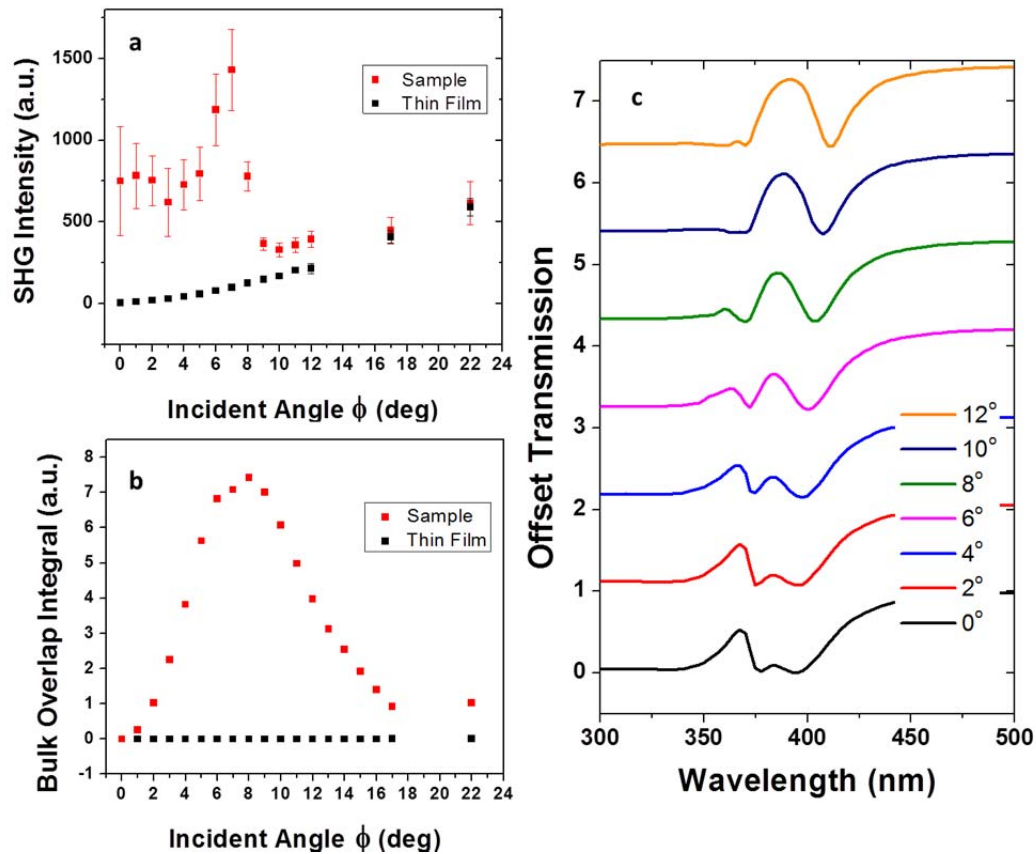
Figure 2.9 – SHG dependence on incident angle. (a) Experimental and (b) simulated angle dependence. (c) Simulated resonace shift with the incidnet angle measured from normal incidence.

While experiment and simulation roughly agree on the peak position for the sample, the signal at low angles is much stronger than predicted, compared to the peak. This is true for both the sample and the thin film. We are still investigating these discrepancies, but one possible explanation could be surface roughness or sample imperfections that break the symmetry but are not considered in the simulations. There are two major factors that could contribute to this strong angle dependence. Firstly, the resonance dependence on coupling between the individual

disks, and is therefore predicted to quickly shifted with changes in the incident angle. A simulation of this resonance shift can be found in (c). Secondly, there is an underlying trend of increasing SHG with increasing angle, due to the thin film behavior that is most likely based on an increase in asymmetry with increasing angle. Overall, it can be said that the sample shows significant enhancement compared to the thin film for lower angles. The SH signal from the thin film quickly increases with incident angles.

Figure 2.10 (a) shows a log-log plot of nonlinear signal with respect to the average laser pump power. The line is a plotted quadratic function; which looks like a linear function with a slope of two in a log-log plot. It can be observed that for peak power densities below 1.5GW/cm^2 the data matches this quadratic trend well. This confirms that the signal depends on the power squared, as expected for a second order process. For larger powers, the signal starts to deviate from the quadratic power dependence. This has been observed before and may be associated with heating[77]. The maximum average power used for this scan was around 1.7mW. Hysteresis was not observed for this power range (see increasing and decreasing power scans in Figure 2.10 (a)), but occurred during further scans with even larger powers. This might be associated with sample damage.

In addition, (b) also gives the conversion efficiency with respect to the average power for the sample and the thin film. It was calculated as $\eta = \frac{P_{FH}}{P_{SH}}$, where P_{FH} and P_{SH} are the average light powers at the fundamental harmonic (FH) and SH, respectively. The average power at the FH was measured with a photodiode based

power meter (Thorlabs S120VC). All optical components were compensated for to the best of my knowledge and abilities. To determine the power at the second harmonic, the efficiency of the PMT must be considered:

$$P_{SH} = \frac{I}{RS(SH) \cdot g \cdot T(SH)}$$

Here, I is the measured PMT anode current in (A); RS(SH) is the radiant sensitivity of the photocathode at 197.6nm in (A/W); g is the gain of the PMT; and T(SH) is the transmission of all optical components in the detection path at the second harmonic wavelength. A maximum conversion efficiency of around $1.2 \cdot 10^{-8}$ was estimated.
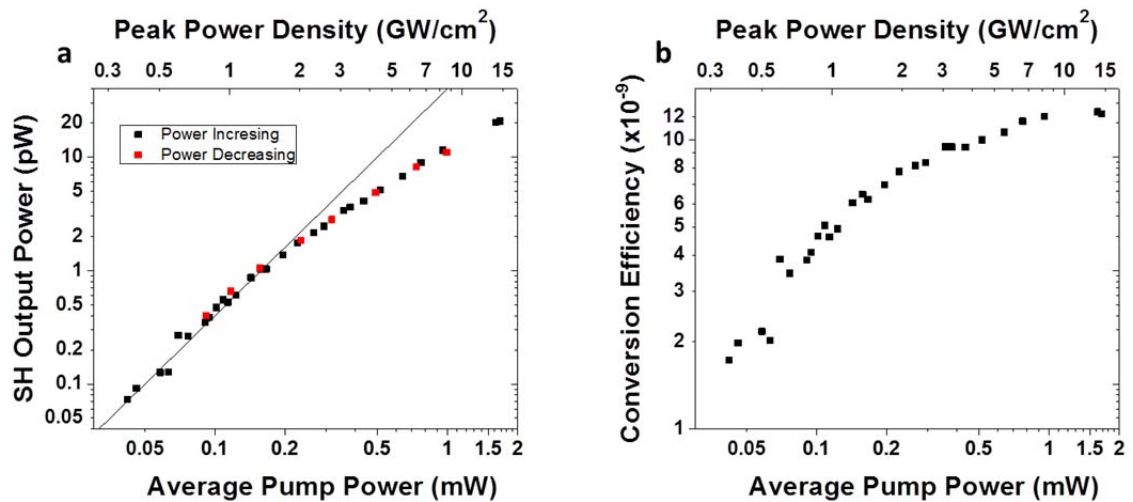
Figure 2.10 – Power dependence. (a) Estimated generated SH power for increasing and decreasing pump powers. (b) Converstion efficiency with respect to pump power.

The conversion efficiency is very low compared to nonlinear crystals. For example, using a KBBF prism coupled device a conversion efficiency of up to 15%

was reported in a similar wavelength regime[61]. However, another way estimate the efficiency of a nonlinear device is by using the effective nonlinear coefficient. It does not only consider the input and output powers, like the conversion efficiency, but also the interaction length. This makes a more inherent comparison with nonlinear crystals possible, since nanostructures and nonlinear crystals have interaction lengths on the nanometer and millimeter scale, respectively. The effective nonlinear coefficient can be defined as[50,78]:

$$d_{eff} = \frac{n_\omega c w_0}{P(\omega)\omega l}\sqrt{\frac{1}{2}\pi n_{2\omega}c\epsilon_0 P(2\omega, l)}$$

Here, ω is the angular frequency at the FH, and, n_ω and $n_{2\omega}$ are the refractive indices at the FH and SH frequency, respectively. w_0 is the beam waist radius. $P(\omega)$ and $P(2\omega, l)$ are the peak powers at the FH and SH frequency, respectively. l is the interaction length; c the speed of light and ϵ_0 the vacuum permittivity. For the ZnO Metamaterial an effective nonlinear coefficient of about 1.0pm/V was calculated, with an incident angle of 7deg from normal. For the bare ZnO thin film at the same angle 0.16pm/V was calculated. For comparison, I also estimated the effective nonlinear coefficient for a KBBF prism coupled device. To do this I assumed a bulk nonlinear coefficient of d_{11} =0.49pm/V [64] for KBBF and calculated the effective coefficient as : $d_{eff} = d_{11}\cos(\phi)$[64]. For the incident angle ϕ I assumed 54deg, which is the phase matching angle at 197nm used in a previous work on a KBBF prism coupled device[61]. Based on these assumptions the effective nonlinear coefficient for a KBBF prism coupled device was calculated as 0.29pm/V. Using this comparison, it

can be observed that the metamaterial performs better than the thin film and the KBBF device. However, for the metamaterial to be used in many practical applications the effective nonlinear coefficient, as well as the conversion efficiency, still need to be improved.

2.5. Summary/Future Work

In summary, using second harmonic generation ultraviolet light with a wavelength of around 197.6-198nm was generated using an all-dielectric metamaterial. To the best of my knowledge this has not been reported before. The patterned ZnO structure has been shown to achieve significant enhancement for lower incident angles. For future work, the near term goal is to further increase the device efficiency, by optimizing the current design maybe. For example, at this point the chromium layer is absorbing part of the nonlinear signal, so an alternative way to make the surface conductive is currently investigated. Another idea is to use an asymmetric structure instead. In addition, an optical cavity could be used to build up the nonlinear signal. In addition, a new metamaterial design could be developed to not just generate but also control the emission of the nonlinear signal, for example focus it. Furthermore, another goal is to move further into the VUV regime, where SHG with crystals becomes more and more difficult.

References

(1)   Tseng, M. L.; Yang, J.; Semmlinger, M.; Zhang, C.; Nordlander, P.; Halas, N. J. Two-Dimensional Active Tuning of an Aluminum Plasmonic Array for Full-Spectrum Response. *Nano Lett.* **2017**, *17* (10).

(2)   Kristensen, A.; Yang, J. K. W.; Bozhevolnyi, S. I.; Link, S.; Nordlander, P.; Halas, N. J.; Mortensen, N. A. Plasmonic Colour Generation. *Nat. Rev. Mater.* **2016**, *2* (1), 16088.

(3)   Olson, J.; Manjavacas, A.; Basu, T.; Huang, D.; Schlather, A. E.; Zheng, B.; Halas, N. J.; Nordlander, P.; Link, S. High Chromaticity Aluminum Plasmonic Pixels for Active Liquid Crystal Displays.

(4)   Proust, J.; Bedu, F.; Gallas, B.; Ozerov, I.; Bonod, N. All-Dielectric Colored Metasurfaces with Silicon Mie Resonators. *ACS Nano* **2016**, *10* (8), 7761–7767.

(5)   Bai, L.; Xie, Z.; Wang, W.; Yuan, C.; Zhao, Y.; Mu, Z.; Zhong, Q.; Gu, Z. Bio-Inspired Vapor-Responsive Colloidal Photonic Crystal Patterns by Inkjet Printing. *ACS Nano* **2014**, *8* (11), 11094–11100.

(6)   Sun, S.; Zhou, Z.; Zhang, C.; Gao, Y.; Duan, Z.; Xiao, S.; Song, Q. All-Dielectric Full-Color Printing with TiO_2 Metasurfaces. *ACS Nano* **2017**, *11* (5), 4445–4452.

(7)   Chen, T.; Reinhard, B. M. Assembling Color on the Nanoscale: Multichromatic

Switchable Pixels from Plasmonic Atoms and Molecules. *Adv. Mater.* **2016**, *28* (18), 3522–3527.

(8)   Duan, X.; Kamin, S.; Liu, N. Dynamic Plasmonic Colour Display. *Nat. Commun.* **2017**, *8*, 14606.

(9)   Genet, C.; Ebbesen, T. W. Light in Tiny Holes. *Nature* **2007**, *445* (7123), 39–46.

(10)   Zhang, J.; Ou, J.-Y.; Papasimakis, N.; Chen, Y.; MacDonald, K. F.; Zheludev, N. I. Continuous Metal Plasmonic Frequency Selective Surfaces. *Opt. Express* **2011**, *19* (23), 23279.

(11)   Kumar, K.; Duan, H.; Hegde, R. S.; Koh, S. C. W.; Wei, J. N.; Yang, J. K. W. Printing Colour at the Optical Diffraction Limit. *Nat. Nanotechnol.* **2012**, *7* (9), 557–561.

(12)   Franklin, D.; Frank, R.; Wu, S.-T.; Chanda, D. Actively Addressed Single Pixel Full-Colour Plasmonic Display. *Nat. Commun.* **2017**, *8*, 15209.

(13)   Olson, J.; Manjavacas, A.; Liu, L.; Chang, W.-S.; Foerster, B.; King, N. S.; Knight, M. W.; Nordlander, P.; Halas, N. J.; Link, S. Vivid, Full-Color Aluminum Plasmonic Pixels. *Proc. Natl. Acad. Sci. U. S. A.* **2014**, *111* (40), 14348–14353.

(14)   Halas, N. J.; Lal, S.; Chang, W.-S.; Link, S.; Nordlander, P. Plasmons in Strongly Coupled Metallic Nanostructures. *Chem. Rev.* **2011**, *111* (6), 3913–3961.

(15)   Franklin, D.; Chen, Y.; Vazquez-Guardado, A.; Modak, S.; Boroumand, J.; Xu, D.; Wu, S.-T.; Chanda, D. Polarization-Independent Actively Tunable Colour

Generation on Imprinted Plasmonic Surfaces. *Nat. Commun.* **2015**, *6* (1), 7337.

(16)   Xu, T.; Walter, E. C.; Agrawal, A.; Bohn, C.; Velmurugan, J.; Zhu, W.; Lezec, H. J.;
       Talin, A. A. High-Contrast and Fast Electrochromic Switching Enabled by
       Plasmonics. *Nat. Commun.* **2016**, *7*, 10479.

(17)   Pryce, I. M.; Aydin, K.; Kelaita, Y. A.; Briggs, R. M.; Atwater, H. A. Highly
       Strained Compliant Optical Metamaterials with Large Frequency Tunability.
       Nano Lett. **2010**, *10* (10), 4222–4227.

(18)   Yang, A.; Hryn, A. J.; Bourgeois, M. R.; Lee, W.-K. K.; Hu, J.; Schatz, G. C.; Odom,
       T. W. Programmable and Reversible Plasmon Mode Engineering. *Proc Natl
       Acad Sci U S A* **2016**, *113* (50), 14201–14206.

(19)   Kamali, S. M.; Arbabi, E.; Arbabi, A.; Horie, Y.; Faraon, A. Highly Tunable Elastic
       Dielectric Metasurface Lenses. *Laser Photon. Rev.* **2016**, *10* (6), 1002–1008.

(20)   Ee, H. S.; Agarwal, R. Tunable Metasurface and Flat Optical Zoom Lens on a
       Stretchable Substrate. *Nano Lett* **2016**, *16* (4), 2818–2823.

(21)   Zheludev, N. I.; Kivshar, Y. S. From Metamaterials to Metadevices. **2012**.

(22)   Song, S.; Ma, X.; Pu, M.; Li, X.; Liu, K.; Gao, P.; Zhao, Z.; Wang, Y.; Wang, C.; Luo,
       X. Actively Tunable Structural Color Rendering with Tensile Substrate. *Adv.
       Opt. Mater.* **2017**, *5* (9), 1600829.

(23)   Yoo, D.; Johnson, T. W.; Cherukulappurath, S.; Norris, D. J.; Oh, S.-H. Template-
       Stripped Tunable Plasmonic Devices on Stretchable and Rollable Substrates.

ACS Nano **2015**, *9* (11), 10647–10654.

(24)   Limonov, M. F.; Rybin, M. V.; Poddubny, A. N.; Kivshar, Y. S. Fano Resonances in Photonics. *Nat. Photonics* **2017**, *11* (9), 543–554.

(25)   Tam, F.; Moran, C.; Halas, N. Geometrical Parameters Controlling Sensitivity of Nanoshell Plasmon Resonances to Changes in Dielectric Environment.

(26)   Jahani, S.; Jacob, Z. All-Dielectric Metamaterials. *Nat. Nanotechnol.* **2016**, *11* (1), 23–36.

(27)   Arsenault, A. C.; Puzzo, D. P.; Manners, I.; Ozin, G. A. Photonic-Crystal Full-Colour Displays. *Nat. Photonics* **2007**, *1* (8), 468–472.

(28)   Kossyrev, P. A.; Yin, A.; Cloutier, S. G.; Cardimona, D. A.; Huang, D.; Alsing, P. M.; Xu, J. M. Electric Field Tuning of Plasmonic Response of Nanodot Array in Liquid Crystal Matrix. *Nano Lett.* **2005**, *5* (10), 1978–1981.

(29)   Lee, Y.; Park, M.-K.; Kim, S.; Shin, J. H.; Moon, C.; Hwang, J. Y.; Choi, J.-C.; Park, H.; Kim, H.-R.; Jang, J. E. Electrical Broad Tuning of Plasmonic Color Filter Employing an Asymmetric-Lattice Nanohole Array of Metasurface Controlled by Polarization Rotator. *ACS Photonics* **2017**, *4* (8), 1954–1966.

(30)   Lauchner, A.; Schlather, A. E.; Manjavacas, A.; Cui, Y.; McClain, M. J.; Stec, G. J.; García de Abajo, F. J.; Nordlander, P.; Halas, N. J. Molecular Plasmonics. *Nano Lett.* **2015**, *15* (9), 6208–6214.

(31)   Stec, G. J.; Lauchner, A.; Cui, Y.; Nordlander, P.; Halas, N. J. Multicolor

Electrochromic Devices Based on Molecular Plasmonics. *ACS Nano* **2017**, *11* (3), 3254–3261.

(32)   Knight, M. W.; King, N. S.; Liu, L.; Everitt, H. O.; Nordlander, P.; Halas, N. J. Aluminum for Plasmonics. *ACS Nano* **2014**, *8* (1), 834–840.

(33)   Huang, Y.-W.; Chen, W. T.; Tsai, W.-Y.; Wu, P. C.; Wang, C.-M.; Sun, G.; Tsai, D. P. Aluminum Plasmonic Multicolor Meta-Hologram. *Nano Lett.* **2015**, *15* (5), 3122–3127.

(34)   Cui, Y.; Zhou, J.; Tamma, V. A.; Park, W. Dynamic Tuning and Symmetry Lowering of Fano Resonance in Plasmonic Nanostructure. *ACS Nano* **2012**, *6* (3), 2385–2393.

(35)   Song, S.; Ma, X.; Pu, M.; Li, X.; Liu, K.; Gao, P.; Zhao, Z.; Wang, Y.; Wang, C.; Luo, X. Actively Tunable Structural Color Rendering with Tensile Substrate. *Adv. Opt. Mater.* **2017**, *5* (9), 1600829–n/a.

(36)   Yoon, J.; Baca, A. J.; Park, S.-I.; Elvikis, P.; Geddes, J. B.; Li, L.; Kim, R. H.; Xiao, J.; Wang, S.; Kim, T.-H.; et al. Ultrathin Silicon Solar Microcells for Semitransparent, Mechanically Flexible and Microconcentrator Module Designs. *Nat. Mater.* **2008**, *7* (11), 907–915.

(37)   Park, S.-I.; Xiong, Y.; Kim, R.-H.; Elvikis, P.; Meitl, M.; Kim, D.-H.; Wu, J.; Yoon, J.; Yu, C.-J.; Liu, Z.; et al. Printed Assemblies of Inorganic Light-Emitting Diodes for Deformable and Semitransparent Displays. *Science* **2009**, *325* (5943),

977–981.

(38)   Huang, N.-T.; Truxal, S. C.; Tung, Y.-C.; Hsiao, A.; Takayama, S.; Kurabayashi, K. High-Speed Tuning of Visible Laser Wavelength Using a Nanoimprinted Grating Optical Tunable Filter. *Appl. Phys. Lett.* **2009**, *95* (21), 211106.

(39)   Ko, H. C.; Stoykovich, M. P.; Song, J.; Malyarchuk, V.; Choi, W. M.; Yu, C.-J.; Geddes III, J. B.; Xiao, J.; Wang, S.; Huang, Y.; et al. A Hemispherical Electronic Eye Camera Based on Compressible Silicon Optoelectronics. *Nature* **2008**, *454* (7205), 748–753.

(40)   Gao, L.; Zhang, Y.; Zhang, H.; Doshay, S.; Xie, X.; Luo, H.; Shah, D.; Shi, Y.; Xu, S.; Fang, H.; et al. Optics and Nonlinear Buckling Mechanics in Large-Area, Highly Stretchable Arrays of Plasmonic Nanostructures. *ACS Nano* **2015**, *9* (6), 5968–5975.

(41)   Gutruf, P.; Zou, C.; Withayachumnankul, W.; Bhaskaran, M.; Sriram, S.; Fumeaux, C. Mechanically Tunable Dielectric Resonator Metasurfaces at Visible Frequencies. *ACS Nano* **2016**, *10* (1), 133–141.

(42)   Di, F.; Hui, Z.; Siyi, X.; Limei, T.; Ningfang, S. Stretchable Array of Metal Nanodisks on a 3D Sinusoidal Wavy Elastomeric Substrate for Frequency Tunable Plasmonics. *Nanotechnology* **2017**, *28* (11), 115703.

(43)   Feng, D.; Zhang, H.; Xu, S.; Tian, L.; Song, N. Fabrication of Plasmonic Nanoparticles on a Wave Shape PDMS Substrate. *Plasmonics* **2016**.

(44)   Kim, T. K.; Kim, J. K.; Jeong, O. C. Measurement of Nonlinear Mechanical Properties of PDMS Elastomer. **2011**.

(45)   Jeong, S. H.; Zhang, S.; Hjort, K.; Hilborn, J.; Wu, Z. PDMS-Based Elastomer Tuned Soft, Stretchable, and Sticky for Epidermal Electronics. *Adv. Mater.* **2016**, *28* (28), 5830–5836.

(46)   Johnston, I. D.; McCluskey, D. K.; Tan, C. K. L.; Tracey, M. C. Mechanical Characterization of Bulk Sylgard 184 for Microfluidics and Microengineering. *J. Micromechanics Microengineering* **2014**, *24* (3), 35017.

(47)   Gaska, R.; Shur, M. S.; Zhang, J. Physics and Applications of Deep UV LEDs. In *ICSICT-2006: 2006 8th International Conference on Solid-State and Integrated Circuit Technology, Proceedings*; 2007; pp 842–844.

(48)   Saleh, B. E. A.; Teich, M. C. *Fundamentals of Photonics*, 2nd ed.; Wiley-Interscience, 2007.

(49)   Boyd, R. W. *Nonlinear Optics*, 2nd ed.; Academic Press, 2003.

(50)   Webb, C. E.; Jones, J. D. C. *Handbook of Laser Technology and Applications*; Institute of Physics, 2004.

(51)   Kauranen, M.; Zayats, A. V. Nonlinear Plasmonics. *Nat Phot.* **2012**, *6* (11), 737–748.

(52)   Franken, P. A.; Hill, A. E.; Peters, C. W.; Weinreich, G. Generation of Optical Harmonics. *Phys. Rev. Lett.* **1961**, *7* (4), 118–119.

(53)   Abe, M.; Awata, N.; Matsushita, T.; Hakamata, M.; Ozawa, K.; Murakami, R.; Shoji, I.; Kondo, T. Accurate Measurement of Quadratic Nonlinear-Optical Coefficients of Zinc Oxide. *J. Opt. Soc. Am. B* **2012**, *29* (9), 2392.

(54)   Kim, S. S.-W.; Jin, J.; Kim, Y.-J. Y.; Park, I.-Y.; Kim, Y.-J. Y.; Kim, S. S.-W. High-Harmonic Generation by Resonant Plasmon Field Enhancement. *Nature* **2008**, *453* (7196), 757–760.

(55)   Boyd, R. W.; Boyd, R. W. Chapter 13 – Ultrafast and Intense-Field Nonlinear Optics. In *Nonlinear Optics*; 2003; pp 533–559.

(56)   Chang, Z.; Rundquist, A.; Wang, H.; Murnane, M. M.; Kapteyn, H. C. Generation of Coherent Soft X Rays at 2.7 Nm Using High Harmonics. *Phys. Rev. Lett.* **1997**, *79* (16), 2967–2970.

(57)   Sivis, M.; Ropers, C. Generation and Bistability of a Waveguide Nanoplasma Observed by Enhanced Extreme-Ultraviolet Fluorescence. *Phys Rev Lett* **2013**, *111* (8), 85001.

(58)   Han, S.; Kim, H.; Kim, Y. W.; Kim, Y. J.; Kim, S.; Park, I. Y.; Kim, S. W. High-Harmonic Generation by Field Enhanced Femtosecond Pulses in Metal-Sapphire Nanostructure. *Nat Commun* **2016**, *7*, 13105.

(59)   CASTECH Inc. http://www.castech.com/productsinfo.aspx?id=122&selectIndex=0 (accessed Feb 12, 2018).

(60) KTP Crystals http://www.newlightphotonics.com/Nonlinear-Optical-Crystals/KTP-Crystals (accessed Feb 12, 2018).

(61) Kanai, T.; Wang, X.; Adachi, S.; Watanabe, S.; Chen, C. Watt-Level Tunable Deep Ultraviolet Light Source by a KBBF Prism-Coupled Device. *Opt. Express* **2009**, *17* (10), 8696.

(62) Chen, C.; Luo, S.; Wang, X.; Wang, G.; Wen, X.; Wu, H.; Zhang, X.; Xu, Z. Deep UV Nonlinear Optical crystal:RbBe_2(BO_3)F_2. *J. Opt. Soc. Am. B* **2009**, *26* (8), 1519.

(63) Guo, S.; Jiang, X.; Liu, L.; Xia, M.; Fang, Z.; Wang, X.; Lin, Z.; Chen, C. BaBe $_2$ BO $_3$ F $_3$: A KBBF-Type Deep-Ultraviolet Nonlinear Optical Material with Reinforced [Be $_2$ BO $_3$ F $_2$] $_\infty$ Layers and Short Phase-Matching Wavelength. *Chem. Mater.* **2016**, *28* (24), 8871–8875.

(64) KBBF Crystals http://www.newlightphotonics.com/Nonlinear-Optical-Crystals/KBBF-Crystal (accessed Feb 13, 2018).

(65) Kauranen, M.; Zayats, A. V. Nonlinear Plasmonics. *Nat. Photonics* **2012**, *6* (11), 737–748.

(66) Shorokhov, A. S.; Melik-Gaykazyan, E. V.; Smirnova, D. A.; Hopkins, B.; Chong, K. E.; Choi, D.-Y.; Shcherbakov, M. R.; Miroshnichenko, A. E.; Neshev, D. N.; Fedyanin, A. A.; et al. Enhanced Third-Harmonic Generation in Silicon Oligomers Driven by Magnetic Fano Resonance. In *Conference on Lasers and*

Electro-Optics; OSA: Washington, D.C., 2016; p FTh3A.3.

(67)   Shcherbakov, M. R.; Neshev, D. N.; Hopkins, B.; Shorokhov, A. S.; Staude, I.;
        Melik-Gaykazyan, E. V; Decker, M.; Ezhov, A. A.; Miroshnichenko, A. E.; Brener,
        I.; et al. Enhanced Third-Harmonic Generation in Silicon Nanoparticles Driven
        by Magnetic Response. *Nano Lett.* **2014**, *14* (11), 6488–6492.

(68)   Staude, I.; Schilling, J. Metamaterial-Inspired Silicon Nanophotonics. *Nat.
        Photonics* **2017**, *11* (5), 274–284.

(69)   Makarov, S. V; Tsypkin, A. N.; Voytova, T. A.; Milichko, V. A.; Mukhin, I. S.; Yulin,
        A. V; Putilin, S. E.; Baranov, M. A.; Krasnok, A. E.; Morozov, I. A.; et al. Self-
        Adjusted All-Dielectric Metasurfaces for Deep Ultraviolet Femtosecond Pulse
        Generation. *Nanoscale* **2016**, *8* (41), 17809–17814.

(70)   Shorokhov, A. S.; Melik-Gaykazyan, E. V.; Smirnova, D. A.; Hopkins, B.; Chong,
        K. E.; Choi, D.-Y.; Shcherbakov, M. R.; Miroshnichenko, A. E.; Neshev, D. N.;
        Fedyanin, A. A.; et al. Multifold Enhancement of Third-Harmonic Generation in
        Dielectric Nanoparticles Driven by Magnetic Fano Resonances. *Nano Lett.*
        2016, *16* (8), 4857–4861.

(71)   Shcherbakov, M. R.; Vabishchevich, P. P.; Shorokhov, A. S.; Chong, K. E.; Choi,
        D.-Y.; Staude, I.; Miroshnichenko, A. E.; Neshev, D. N.; Fedyanin, A. A.; Kivshar,
        Y. S. Ultrafast All-Optical Switching with Magnetic Resonances in Nonlinear
        Dielectric Nanostructures. *Nano Lett.* **2015**, *15* (10), 6985–6990.

(72)   Makarov, S. V.; Petrov, M. I.; Zywietz, U.; Milichko, V.; Zuev, D.; Lopanitsyna, N.; Kuksin, A.; Mukhin, I.; Zograf, G.; Ubyivovk, E.; et al. Efficient Second-Harmonic Generation in Nanocrystalline Silicon Nanoparticles. *Nano Lett.* **2017**, *17* (5), 3047–3053.

(73)   Grinblat, G.; Li, Y.; Nielsen, M. P.; Oulton, R. F.; Maier, S. A. Enhanced Third Harmonic Generation in Single Germanium Nanodisks Excited at the Anapole Mode.

(74)   Liu, S.; Sinclair, M. B.; Saravi, S.; Keeler, G. A.; Yang, Y.; Reno, J.; Peake, G. M.; Setzpfandt, F.; Staude, I.; Pertsch, T.; et al. Resonantly Enhanced Second-Harmonic Generation Using III–V Semiconductor All-Dielectric Metasurfaces. *Nano Lett.* **2016**, *16* (9), 5426–5432.

(75)   Miroshnichenko, A. E.; Evlyukhin, A. B.; Yu, Y. F.; Bakker, R. M.; Chipouline, A.; Kuznetsov, A. I.; Luk'yanchuk, B.; Chichkov, B. N.; Kivshar, Y. S. Nonradiating Anapole Modes in Dielectric Nanoparticles. *Nat. Commun.* **2015**, *6*.

(76)   O'Brien, K.; Suchowski, H.; Rho, J.; Salandrino, A.; Kante, B.; Yin, X.; Zhang, X. Predicting Nonlinear Properties of Metamaterials from the Linear Response. *Nat. Mater.* **2015**, *14* (4), 379–383.

(77)   Grinblat, G.; Li, Y.; Nielsen, M. P.; Oulton, R. F.; Maier, S. A. Enhanced Third Harmonic Generation in Single Germanium Nanodisks Excited at the Anapole Mode. *Nano Lett.* **2016**.

(78)   Eckardt, R. C.; Byer, R. L. Measurement of Nonlinear Optical Coefficients by Phase-Matched Harmonic Generation; Bordui, P. F., Ed.; International Society for Optics and Photonics, 1991; Vol. 1561, pp 119–127.